www.elsevier.com/locate/memsci

Poly(2,5-benzimidazole)/Sulfonated Sepiolite Composite Membranes with Low Phosphoric Acid Doping Levels for PEMFC Applications in a Wide Temperature Range

Xiaoxiao Zhang, Qingting Liu, Lei Xia, Dongyang Huang, Xudong Fu, Rong Zhang, Shengfei Hu, Feng Zhao, Xiao Li, Xujin Bao

PII: S0376-7388(18)32662-0
DOI: https://doi.org/10.1016/j.memsci.2018.12.085
Reference: MEMSCI16768

To appear in: *Journal of Membrane Science*

Received date: 23 September 2018
Revised date: 26 December 2018
Accepted date: 30 December 2018

Cite this article as: Xiaoxiao Zhang, Qingting Liu, Lei Xia, Dongyang Huang, Xudong Fu, Rong Zhang, Shengfei Hu, Feng Zhao, Xiao Li and Xujin Bao, Poly(2,5-benzimidazole)/Sulfonated Sepiolite Composite Membranes with Low Phosphoric Acid Doping Levels for PEMFC Applications in a Wide Temperature Range, *Journal of Membrane Science,* https://doi.org/10.1016/j.memsci.2018.12.085

Poly(2,5-benzimidazole)/Sulfonated Sepiolite Composite Membranes with Low Phosphoric Acid Doping Levels for PEMFC Applications in a Wide Temperature Range

Xiaoxiao Zhang[a,b], Qingting Liu[a,b,*], Lei Xia[a], Dongyang Huang[a], Xudong Fu[a,b], Rong Zhang[a,b], Shengfei Hu[a,b], Feng Zhao[b,c], Xiao Li[b,c], Xujin Bao[b,d,*]

[a]School of Materials and Chemical Engineering, Hubei University of Technology, Wuhan, 430068, China

[b]Hubei Provincial Key Laboratory of Green Materials for Light Industry, Hubei University of Technology, Wuhan, 430068, China

[c]Wuhan Troowin Power System Technology Co., Ltd., Wuhan, 430079, China

[d]Department of Materials, Loughborough University, Leicestershire, LE11 3NW, UK

[*]liuqt@hbut.edu.cn

X.Bao@lboro.ac.uk

Abstract

To broaden the operating temperature range of phosphoric acid (PA) doped polybenzimidazole membrane-based proton exchange membrane fuel cells (PEMFCs) toward low temperatures, a novel series of poly(2,5-benzimidazole) (ABPBI)/sulfonated sepiolite (S-Sep) composite membranes (ABPBI/S-Sep) with low PA doping levels (DLs) were prepared via *in-situ* synthesis. The desirably enhanced mechanical, thermal, and oxidative stabilities of ABPBI/S-Sep composite membranes were achieved by constructing ABPBI chains arranged along the sepiolite (Sep) fibers

and acid-base crosslinks formed between S-Sep fibrous particles and ABPBI chains. Benefiting from the richness of high temperature stable bound water and the excellent water absorbability of Sep particles that enable the formation of additive proton conducting paths, the composite membranes retained bounded PA and achieved much higher proton conductivities under both anhydrous and hydrous conditions compared to PA-doped ABPBI membranes. Proton conductivity values above 0.01 S/cm at 40-90 °C/20-98% RH conditions and 90-180 °C/anhydrous conditions as well as peak power density of 0.13 and 0.23 W/cm^2 at 80 and 180 °C with 0% RH, respectively from the ABPBI/2S-Sep composite membrane are more holistic compared to Nafion at low temperatures and polybenzimidazole-based membranes at high temperatures, respectively. The excellent properties of ABPBI/S-Sep composite membranes suggest them as prospective candidates for PEMFCs applications in a wide temperature range.

Keywords: Proton exchange membrane; Poly(2,5-benzimidazole); Sepiolite; Proton conductivity; Wide temperature range

1. Introduction

During the last few decades, proton exchange membrane fuel cells (PEMFCs) have attracted significant attention as green and efficient energy devices, featuring high energy conversion efficiency, environment-friendliness, and quick start-up [1-3]. Two types of PEMFCs exist according to the operating temperatures: low temperature (LT) (< 100 °C) and high temperature PEMFC (HT-PEMFC) (100-200 °C). The traditionally developed PEMFC based on the use of perfluorosulfonated polymer membranes (e.g. Nafion) is assigned to LT-PEMFC and suffers from two main

limitations: critical operating conditions (e.g., an operating temperature below 100 °C and a relative humidity (RH) above 80%) and high cost [1, 4]. In contrast, phosphoric acid doped polybenzimidazole (PA-PBI) is the only membrane material that meets the criteria for HT-PEMFC applications required by the US Department of Energy (DOE). Nonetheless, a PA-PBIs (PBI and its derivatives) proton exchange membrane (PEM) based PEMFC is still limited to applications in a constrictive temperature range of 120-180 °C to avoid PA leaching in hydrous atmosphere and degradation above 180 °C [5-8]. PEMFCs operating at wider temperatures, especially covering LT and HT ranges under various relative humidity (RH) (or without any external humidification system) are highly desirable [9-11]. Recently, Lee et al. [12] reported a novel class of PEMs based on PA-doped QAPOH (quaternary ammonium-biphosphate ion-pair-coordinated polyphenylene) and these fuel cells exhibit stable performance at 80-160 °C. However, PEMs with high performances over wider temperatures (i.e., from room temperature to 200 °C under a low RH or uncontrolled humidity conditions) have not been reported to date.

To realize a PEM with high performances under such demanding conditions, it is necessary to consider two design aspects: high performance polymer and optimal proton conducting path design. In general, the long-term operating temperature for a PEM material is below its glass transition temperature (T_g). Nafion and most aromatic polymers (as PEM candidates) have T_g values below 200 °C, and their thermomechanical and chemical oxidation stabilities deteriorate after sulfonation treatment [13]. A reasonable proton conductivity for a PEM at the wide temperature range with various RH is extremely important [14]. Proton conducting through a PEM is explained by vehicle (H_3O^+) and Grotthuss (proton hopping) mechanisms. The former is mainly observed to be proton conducting as a H_3O^+ vehicle through

hydrophilic tunnels in a sulfonated polymer membrane under hydration conditions [15]. The latter is mainly considered as proton hopping between acid molecules in an acid doped membrane (typically PA-PBI) under anhydrous conditions [16]. Since proton conduction is mediated through portable water molecules via vehicle mechanism, sulfonated polymer membranes face at least two critical challenges. Firstly, they must remain humid to obtain high proton conductivity. However, on the one hand, with the operation temperature increasing to 200 °C, the consequently required saturated water vapor pressure as high as 15 atm, will greatly increase the complexity of the system construction if high RH is to be achieved during operation [6]; on the other hand, the hydrophilic channels for water migration will be destroyed when a PEM operates at elevated temperatures close to their T_g, resulting in dramatically decreased proton conductivity [13]. Secondly, they must obtain a maximum possible sulfonation degree to ensure reasonably high proton conductivity which is vital to run at high temperature and low humidity conditions. Unfortunately, both conductivity and water uptake heavily depend on the concentration of proton conducting units (most commonly sulfonic acid) and a high sulfonation degree will greatly damage the mechanical and thermal stability as well as fuel impermeability. As a result, such sulfonated polymer membranes are inefficient for HT-PEMFC operation up to 200 °C.

Compared to sulfonated polymer candidates, PA-PBIs has better comprehensive properties for wider temperature applications although it still has defects. It is worth mentioning that the operating temperature range of 120-180 °C for the PA-PBIs PEM is not limited by PBIs but free PA, since PBIs as a kind of fully aromatic heterocyclic resins have adequate thermal and chemical stabilities for HT application. Only when doped with PA with high DLs, the PBIs-based membranes exhibit reasonable proton

conductivity for HT-PEMFC. Theoretically, an imidazole (Im) group in a PBI chain binds a PA molecule, in other words, the saturated PA DL value of PBI is 2[17]. The practical PA DL of PA-PBI membrane is much higher than 2 and this is due to the so-called free PA. For an ideal temperature range of 120-180 °C for PA-PBIs based HT-PEMFC, the lower boundary temperature of 120 °C is suggested to avoid the formation of water, which would result in free PA leaching. However, the upper boundary level of 180 °C avoids free PA degradation, which will both dramatically decrease the proton conductivity and deteriorate the performance of the resulting fuel cells [18, 19]. It has also been reported that the mechanical strength and dimensional stability of PBI membranes greatly decreased with high PA DLs [20].

Many reviews have comprehensively summarized the development of PBI-based PEMs [6, 19, 21-23]. Significant efforts have been focused on increasing the PA retention capability while reducing PA leaching to improve the PA-PBI based HT-PEMFC performance. For instance, incorporating of insoluble proton conductors [24, 25] or anchoring the soluble proton conductors onto insoluble matrix [26, 27] can solve the PA leaching problem to some extent. However, the purpose of PA-PBI based PEMs for application in LT conditions have rarely been concerned about. As discussed above, the real obstacle is the free PA leaching problem discussed above and the relatively low conductivity under LT conditions. Schmidt [28, 29] and Molleo et al. [5] have summarized the effects of PA leaching on membrane electrode assembly (MEA), component degradation, and system performance. Firstly, the free PA leaching out of a membrane can not only dramatically decrease the proton conductivity and mechanical strength of a membrane, but also cause fuel loss and short cuts due to membrane thinning and pin-hole formation. Secondly, the exudative PA will poison the Pt-metal catalyst and destroy the interface between the membrane

and the catalyst layer, resulting in an irreversible damage of the MEA. Finally, PA dissolving in the aqueous solution will corrode the components of a PEMFC including carbon, the gas diffusion layer, and metal parts. Therefore, to drive PA-PBI-based PEM spreading in LT applications, it is necessary to design additive proton conducting paths that are independent of conducting protons through massive-free PA.

Amongst these approaches on PEMs for HT-PEMFCs, organic-inorganic composite membranes have attracted significant interest mainly due to their improved proton conductivity and enhanced thermomechanical properties, as well as favorable commercializing prospects such as industrial manufacture and low cost [30]. Kim et al. [22] have summarized the previous efforts in this field. Through incorporation of inorganic fillers into an sulfonated polymer or an acid-doped PBI matrix, such as hygroscopic inorganic oxides (SiO_2, TiO_2, ZrO_2, and Al_2O_3), polyhedral oligomeric silsesquioxane (POSS), heteropolyacids, and carbonaceous materials, the obtained organic-inorganic composite membranes generally show good thermomechanical strength and enhanced water and/or acid retention capability, thus improving proton conductivity at HT under low RH conditions [6, 21, 31]. Since clay-reinforced polymer composites are renowned for their good mechanical strength, modulus, as well as dimensional, thermal, and chemical stability, these composites are expected to produce more dimensionally stable membranes at low cost [32]. In relevant studies, natural minerals with micro- or nano-size porous, laminar, or channeled structures, such as sepiolite [33-37], bentonite [38], laponite [32, 39], montmorilonite [40, 41], and palygorskite [42] have been reported for the preparation of PEMs. The results indicate that high proton conductivities can be achieved by additional proton transfer through the absorbed or bound water molecules in clays via vehicle and/or Grotthuss

mechanisms.

Here, a proton conduction multipath was used based on PA doped ABPBI incorporated with sulfonated sepiolite particles (S-Sep) composite membranes (ABPBI/S-Sep). Sep is a type of porous fibrous clay mineral that has attracted significant interest due to its unique physical structure that includes a high specific surface area, micro-porous channels (0.35-1.06 nm) that run parallel to its length [43], and excellent water absorbability and maintenance [34]. Due to its natural capacity for excellent hygroscopicity, Sep has been used to improve the mechanical properties and proton conductivity of Nafion/Sep composite membranes at high temperature and low RH [33, 34]. For its application in a wider temperature range without humidity control, several potential advantages are available with this approach. Through incorporation of the hygroscopic Sep with excellent water absorbability and maintenance at HT conditions, S-Sep particles in composite membranes provide new proton paths through internally bound water to offset the insufficient proton conductivity under low PA DLs. While, proton paths crossing the boundary of inorganic and organic components are provided by hydrogen links between sulfonic acid grafted onto Sep surfaces and PA and Im groups in PA-ABPBI. Additionally, proton can transfer through absorbed moistures at LT with high RH conditions. As a result, protons are expected to be efficiently delivered through the composite membrane under various temperature and humidity conditions.

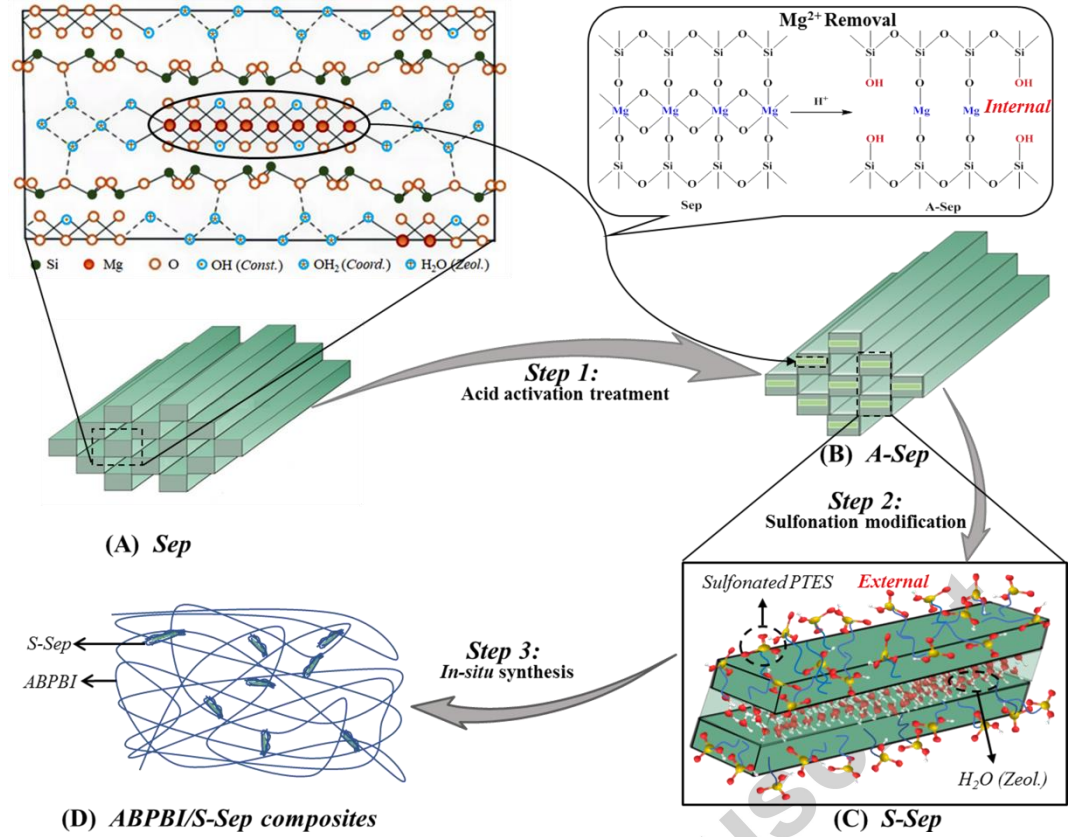

Fig. 1 Schematic representation of a Sep fiber and its surface modification as well as its *in-situ* synthesis process (A, Sep fiber; B, A-Sep; C, S-Sep; D, ABPBI/S-Sep composites).

In the present work, a series of ABPBI/S-Sep composite membranes with low PA DLs were successfully utilized to improve proton conductivity and reduce PA leaching to achieve wide temperature operation of PEMFCs. A schematic illustration of the preparation of ABPBI/S-Sep composites is presented in Fig. 1. The rich combined water with high temperature maintenance that exists in zeolitic channels (as shown in the partial view of Sep in Fig. 1A) is expected to form additional proton paths. In step 1, the enlarged internal and external surface area was achieved via acid activation treatment with effects of defibration and magnesium removal [44-46] (Fig. 1B). Typically, the incorporation of inorganic nanoparticles into a PBI-based membrane may cause phase separation, thus resulting in decreased mechanical strength and proton conductivity [47]. Therefore, the nano-sized Sep particle after defibration was modified by a silane coupling agent in step 2, followed by sulfonation

treatment to achieve S-Sep according to Beauger et al. [34] (Fig. 1C). In step 3, ABPBI/S-Sep composites with uniformly dispersed S-Sep were achieved via *in-situ* synthesis. Finally, ABPBI/S-Sep composite membranes with low PA DLs will be obtained by using a solution casting method followed by PA doping and washing procedures. The effects of acid activation and sulfonation treatments on Sep particles, as well as the structures and properties of ABPBI/S-Sep composite membranes were systematically investigated. Due to the combination of the detailed relevant functions of the S-Sep filler, this work realized that composite membranes can operate in a wider temperature range covering LT and HT. In fact, the excellent performance of ABPBI/S-Sep composite membranes with thermomechanical and oxidation stabilities and comparable proton conductivities with commercial Nafion at LT and PBIs membranes with high PA DLs at HT was achieved. This study contributes a feasible method for the fabrication of a new class of PEMs for operation in a wide temperature range and without the requirement of additional humidifiers.

2. Experimental

2.1 Raw Materials

Sep, a natural fibrous clay mineral, was kindly supplied by Xiangtan Yuanyuan Sepiolite New Material Co., Ltd., China. 3,4-Diaminobenzoic acid (DABA, 98.0%) was purchased from Beijing J&K Technology Co., Ltd., China. Methane sulfonic acid (MSA, 99.0%) and phenyltriethoxysilane (PTES, 99.0%) were purchased from the Aladdin Industrial Corporation, USA. P_2O_5 (98.0%), PA (85.0%), NaOH (85.0%), isopropanol (99.7%), HCl (36.0-38.0%), fuming sulfuric acid (H_2SO_4, 20% free SO_3 basis), H_2O_2 (30.0%), $FeSO_4 \cdot 7H_2O$ (99.0%), and ethanol (99.7%) were purchased

from Sinopharm Chemical Reagent Co., Ltd., China. All chemicals were used without further purification.

2.2 Preparation and characterization of sulfonated Sep particles

2.2.1 Acid activation treatment

10.0 g of Sep and a specific concentration (0.5, 1.0, 1.5, 2.0, or 2.5 M, respectively) of HCl solution at a liquid-solid ratio of 10:1 (mL/g) were magnetically stirred and heated at 80 °C for 8 h; then, the obtained suspensions were filtered and washed thoroughly with deionized water until the filtrates were neutral and then dried at 110 °C for 24 h to obtain acid activated Sep (abbreviated as A-Sep). The prepared samples are designated as A-Sep-0.5M to A-Sep-2.5M according to the concentration of HCl used in the acid activation treatment.

2.2.2 Coupling agent modification

Isopropanol (17 mL), HCl (3 mL), and A-Sep-2.0M (1.0 g) were mixed under magnetic stirring; then, 0.6 g PTES was added after ultrasonic homogenization. The mixture was heated at 65 °C for 15 h, then successively filtered and washed with ethanol and deionized water after desiccation to obtain PTES modified particles (A-Sep-PTES). The yield of PTES coupling agent modification treatment is about 95%.

2.2.3 Sulfonation modification

The sulfonation process was conducted according to Beauger et al. [34]. 50.0 g of excess fuming H_2SO_4 solution was added to all A-Sep-PTES product obtained in the previous step and heated at 80 °C under stirring for 24 h; then, the solution was purified and dried to obtain sulfonated particles (S-Sep). The yield of sulfonation modification treatment is about 80%.

2.2.4 Characterization of Sep particles

The specific surface area and pore structure of nano-fibrous Sep were analyzed by N_2 adsorption-desorption isotherms (ASAP 2020 plus HD88, Micromeritics Instrument (Shanghai) Co., Ltd., China) measured at -196 °C. Prior to the adsorption-desorption tests, samples were degassed at 150 °C for 24 h.

The content of Mg^{2+} in Sep samples was determined via Inductively Coupled Plasma Emission Spectroscopy (ICP-OES) (Perkin Elmer, Optima 5300 DV, USA), and the removed Mg^{2+} was calculated with the following equations (removed Mg^{2+} (%)= ($W_{Sep} - W_{A\text{-}Sep}$) / W_{Sep} × 100), where W_{Sep} represents the Mg^{2+} content in Sep and $W_{A\text{-}Sep}$ represents the residual Mg^{2+} content in A-Sep samples after acid activation treatment.

The crystal structures of fibrous Sep samples before and after acid activation treatment were characterized via XRD (Empyrean type XRD analyzer, PANalytical B.V., Netherlands) over a range of $5° \leq 2\theta \leq 50°$, using a Cu Kα X-ray source (40 kV, 40 mA). Morphological analysis was conducted via TEM (Tecnai G2 20, FEI, USA).

The static contact angle between Sep samples and deionized water was measured via contact angle meter (JC2000D, Shanghai zhongchen digital technic apparatus Co., Ltd., China) to investigate the change of hydrophilicity of samples before and after surface modification.

The chemical structures of Sep particles before and after acid activation and surface modification were characterized via FTIR (Tensor 2, Bruker, USA).

The titration measurement of S-Sep sample was carried out according to previous reports by Beauger et al. [34]. Fully protonated S-Sep was immersed in 50 mL of 0.001 M NaOH to replace the H^+ of the $–SO_3H$; the remaining $OH^–$ were then titrated with 0.001 M HCl, thus calculating the number of exchanged protons. The ion exchange capacity (IEC) of the S-Sep sample is expressed as the number of millimoles of protons exchanged per gram of dry S-Sep (meq/g); the IEC result of the S-Sep was the average of three samples.

2.3 Preparation and characterization of ABPBI/S-Sep composite membranes

2.3.1 Synthesis of composites

3.0 g of monomer DABA, 6.0 g of P_2O_5, calculated amounts (1, 2, 3, and 5 wt.%, respectively) of S-Sep and 20 ml of MSA were added to a 100 mL three-neck flask and ultrasonicated for 2 h to obtain a homogeneous suspension. The suspension was heated under N_2 atmosphere and magnetic stirring at 100 °C for 30 min; then, the suspension was continuously heated at 150 °C for 2 h. The hot composite suspension was slowly poured into the deionized water to obtain very thin fibers. The obtained

fibers were firstly boiled in a beaker with 10% NaOH solution at 100 °C for 2 h to remove the remaining MSA and PA, subsequently boiled in deionized water to remove NaOH. Repetition of alternatively boiling in NaOH and deionized water may be necessary to remove residual acid and NaOH to the greatest extent. Finally, the fibers were dried in a vacuum oven at 110 °C for 24 h to obtain the ABPBI/S-Sep composite.

2.3.2 Membranes casting

0.4 g of the ABPBI/S-Sep composite was dissolved in 6 mL of MSA under magnetic stirring overnight at room temperature to obtain a homogeneous suspension. Then, the viscous suspension was cast onto a flat bottom petri dish and the solvent was removed by heating in a ventilated oven at a maximum temperature of 200 °C. After cooling to room temperature, the petri dish was immersed into deionized water to peel off the membrane. The membrane was then dried in a vacuum oven at 110 °C for 24 h to obtain the ABPBI/S-Sep composite membrane, which was abbreviated ABPBI/XS-Sep. X represents X wt.% of S-Sep particles in the composite membrane. The virgin ABPBI membrane was prepared by evaporating MSA solvent under the same conditions. The thicknesses of all membranes were 40-55 μm. The synthesis and membrane casting method of ABPBI was identical to ABPBI/S-Sep composites, except that no S-Sep inorganic particles were added during the synthesis process.

2.3.3 Preparation of phosphoric acid doped membranes

The membranes were dried at 110 °C for 24 h in a vacuum oven until they reached a constant weight; then, they were immersed into different concentrations of phosphoric acid solution (40-80%, mass fraction) for 3 d at room temperature, and then rinsed with deionized water to eliminate free PA on the surface. After that, membranes were dried at 110 °C in a vacuum oven for 24 h to obtain PA doped membranes with different PA DLs For the preparation of a PA doped membrane with free PA removal to measure the proton conductivity, the composite membrane was boiled in deionized water for 3 h and then dried at 110 °C in a vacuum oven for 24 h.

2.3.4 Characterization of membranes

With the introduction of S-Sep, the effects on chemical and crystal structures, fracture morphologies, mechanical properties, and thermal stabilities of composite membranes were observed via XRD, FESEM, DMA, and TGA, respectively. The essential properties for a PEM, including chemical and dimensional stabilities, water and PA absorbabilities, retention capabilities, and proton conductivity, were measured by widely employed methods according to references.

A FESEM (QUANTA, FEG450, USA) coupled with Energy Dispersive X-ray Spectroscope (EDS) was used to perform the membrane fracture surface characterization and distribution of elements. The samples were coated with a layer of gold prior to measurement to increase electrical conduction. The mechanical properties of the membranes were obtained via DMA and tensile tests. DMA was

conducted with a Q800 DMA (TA instruments, USA) at a heating rate of 3 °C/min from 25 to 300 °C at a sinusoidal frequency of 1 Hz and 0.1% strain. Tensile test was conducted with an Electronic Universal Testing Machine (CMT4204, Mester, China) at a tensile speed of 50 mm/min under ambient atmosphere. The obtained results represent the average of five samples each of which with a size of 10×2.5 mm. TGA was examined in a temperature range of 30-800 °C under N_2 atmosphere at a heating rate of 10 °C/min with a thermal analyzer (SDT Q600, TA instruments, USA).

The oxidative stability of the membranes was evaluated via immersion in Fenton's reagent (3% H_2O_2 containing 4 ppm Fe^{2+}) for 5 d at 70 °C. Prior to dipping in Fenton's solution, the accurate weight of the dried membranes was noted (W_0). Then, the membranes were taken out at 24 h intervals, dried at 110 °C in a vacuum oven for 12 h and their weights were measured again (W_i). Then, the membranes were re-immersed in the fresh Fenton's reagent. Their oxidative stability was measured as the remaining weight percentage after taking the membranes out of Fenton's reagent.

The measurement and calculation for water uptake and PA DL of a membrane refer to previously published equations [48]. The water uptake measurement was performed by putting dried membranes (dried at 110 °C in a vacuum oven for 24 h until they reached a constant weight) in deionized water at room temperature for 24 h.

Acid retention, swelling ratio, and swelling volume measurements of ABPBI and ABPBI/S-Sep composite membranes were conducted according to previous reports [20, 49, 50]. All membranes were first completely dried in a vacuum oven at 110 °C for 24 h and their weights and dimensions in *x*, *y*, and *z* direction were noted. The

PA-doped membranes were repeatedly rinsed with deionized water and then mopped with filter paper to remove surficial water and PA; then, their weights (W_0) and dimensions were measured again. The swelling ratio and swelling volume were calculated using the following equations (swelling area = (S_w - S_d) / S_d × 100 %, S = x × y; swelling volume = (V_w - V_d) / V_d × 100 %, V = x × y × z), where S_d and S_w is the area of the dry and wet membranes, respectively; V_d and V_w is the volume of the dry and wet membranes, respectively. They were then hanged over boiling water for 5 h and the weights of the membranes (W_i) were measured every 20 min during the first hour and then every 60 min after wiping off the acid that leached from the membranes. The weight loss ratio of PA in the membranes was calculated using the formula (R = (W_0 - W_i) / W_a), Where, W_0 represents the initial weight of the PA doped membranes, W_i represents the weight of the membranes after each hour of leaching, and W_a represents the original weight of PA present in the membranes calculated from PA DL measurements.

The impedance spectra were obtained via a two-electrode AC impedance spectroscopy (PARSTAT 4000, Princeton, USA) and an environmental test chamber (LP-80U, Guangdong Hongzhan tech, China). The impedance spectra were recorded from 4 MHz to 1 Hz. The samples were sandwiched between two circular platinum (Pt) electrodes (diameter 10.0 mm, purity 99.95%, Tianjin Leiruite Instrument and Meter Sales Co., Ltd.), and were fixed firmly into a PEEK cell with two springs. The cell was then placed into an environmental test chamber to conduct the impedance measurement under different temperature and humidity conditions. The through-plane

proton conductivity (σ) was calculated from the measured current resistance (R) using the equation ($\sigma = L / (R \times A)$), where, σ, L, R, and A, represent proton conductivity (S/cm), distance between two electrodes, i.e. membrane thickness (cm) in this case, resistance from the impedance data (Ω), and cross-sectional area (cm^2) of the membranes, respectively.

2.3.5 Single cell test

Gas diffusion layer (carbon paper, Avcarb GDS2240) incorporated with wet proofed micro-porous layer (H2315 T10AC1) obtained from Freudenburg (FFCCT, Germany) were used as substrates with size of 1 cm^2 to deposit the catalyst layer for the electrode. The catalyst inks were prepared by blending catalysts (20 wt.% Pt/C, Alfa Aesar) in a water/ethanol mixture and ultrasonic vibrated for 1 h. Then, the catalyst inks were sprayed onto carbon substrates at 100 °C, and the electrodes were held at 150 °C for 2 h to remove residual solvent. The Pt loadings on the cathode and anode were both 0.4 mg/cm^2. The MEA was finally obtained by hot pressing the electrodes onto PA doped membranes at 5 MPa for 3 min at 120 ºC. Dry H_2 and O_2 were fed into the cell at flow rates of both 200 cm^3/min. To ensure the steady state, the cell was held at each desired conditions for 1 h before performing the measurements.

3. Results and Discussion

3.1 Modification of Sep particles

A strategy for Sep functionalization was employed mainly according to Beauger

et al. [34]. This strategy based on three steps is presented in Fig. 1. Step 1 is the acid activation treatment that achieves Sep fibrous particles with extended surface area and a large number of exposed Si–OH groups. Step 2 introduces phenyltriethoxy groups onto Sep via silanol condensation between Sep and PTES. Step 3 is a sulfonation process that forms a hydrophilic sulfonated benzene ring to promote the compatibility between Sep particles and ABPBI matrix.

3.1.1 Acid activation

Natural Sep is a clay mineral and generally contains impurities such as metal ions and small pores with low specific surface area, which must be ameliorated before use in composites. Acid activation treatment of Sep fibrous particles generally results in purification and defibration as well as improvements of specific surface area and porosity. The results of relative measurements are shown in Fig. 2, Fig. 3 and Table 1, respectively.

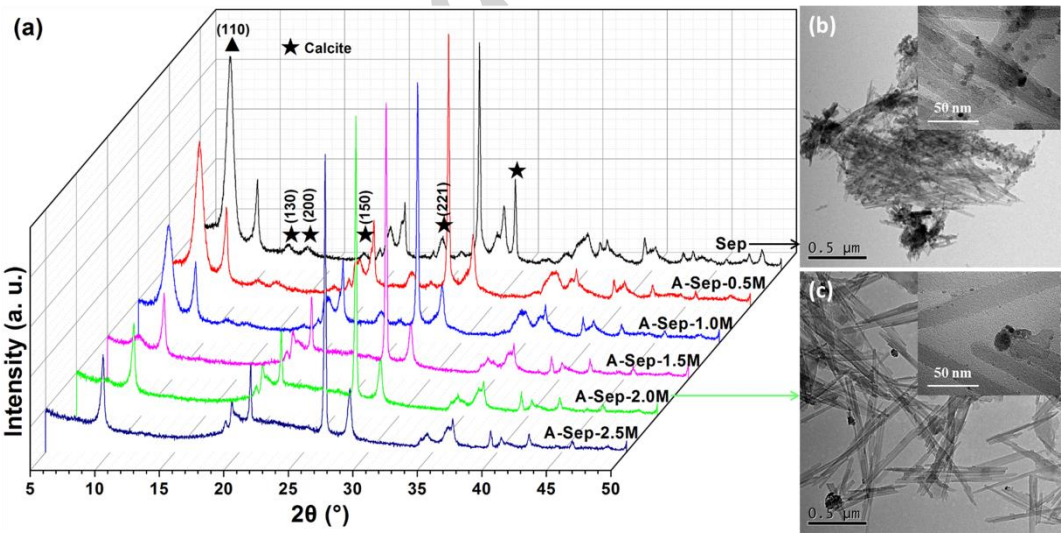

Fig. 2 XRD spectra of Sep and A-Sep particles (a) and TEM images of Sep (b) and A-Sep-2.0M (c).

The XRD spectra of Sep particles before and after acid treatment with HCl at

various concentration are presented in Fig. 2a. All samples show typical characteristic diffraction peaks of Sep particles at 2θ = 9.45°, 20.84°, 26.64°, and 28.54°, which correspond to an orthorhombic crystalline system, indicating an undamaged crystalline structure after acid activation treatment [51]. In Table 1, 11.16% of the measured Mg^{2+} content of raw Sep, which is lower than the theoretical content (e.g. 14.86%), indicates 3.70% impurities. The intensity of peaks from calcite impurities (marked with the symbol "★" in Fig. 2a) gradually decreased with increasing HCl concentration to 1.0 M and subsequently disappeared in response to continuously increasing HCl concentration from 1.5 M to 2.5 M. The changes of XRD spectra as well as the results of FTIR spectra shown in Fig. 5, clearly confirm the effect of impurity (mainly are metal ions, such as K^+, Na^+, Ca^{2+} and so on) removal [45] and also indicate that the ideal HCl concentration should be above 1.0 M. Moreover, the untreated Sep particles are agglomerated and can be separated by HCl treatment under hydrothermal environment [45, 46], which is also evidently confirmed by TEM measurement. The heavy agglomeration of raw Sep particles as shown in Fig. 2b clearly show the well separated Sep fibers with a nano-scale of length 200 nm to 1 μm and a diameter about 20 nm (in Fig. 2c).

In a XRD spectrum of Sep, the 2θ = 7.32° characteristic peak is related to the (110) plane of the Sep lattice [46]. In Fig. 2a, this declines dramatically in samples A-Sep-1.5M and A-Sep-2.0M, while it almost disappeared in sample A-Sep-2.5M. This is because the magnesium octahedral sheet between two layers of silica tetrahedrons has been holed due to the Mg^{2+} removal. To further confirm this, a

measurement of Mg^{2+} content was employed by ICP-OES and the results of removed Mg^{2+} are shown in Table 1. Only 5.56% and 11.12% of Mg^{2+} were removed for A-Sep-0.5M and A-Sep-1.0M, respectively. With HCl concentration increasing beyond 1.0 M, the removed Mg^{2+} jumped to 42.11% and beyond. Clearly, almost half of the amount of Mg^{2+} was replaced by H^{+} from HCl according to the reaction illustrated in step 1 in Fig. 1 [44], which resulted in a penetrated internal channel in Sep particles (as schematically illustrated in Fig. 1B).

With the exception of evidence for the removal of a large amount of Mg^{2+} in combination with K^{+}, Na^{+}, Ca^{2+}, and other impurities in Sep particles, the changes of specific surface area and the pore volume of the micro-pores by acid treatment can be efficiently detected through BET test [45, 52].

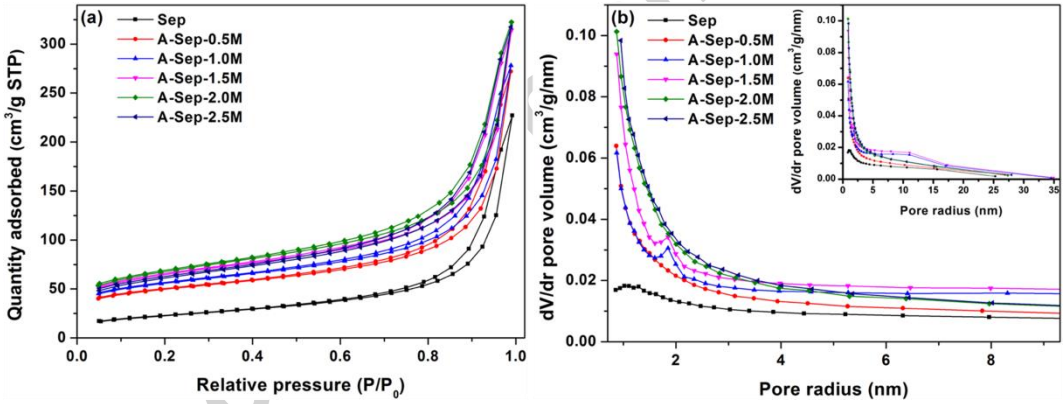

Fig. 3 N_2 adsorption-desorption isotherms (a) and pore size distribution plots (b) of Sep and A-Sep particles.

Table 1 BET specific surface area, pore structure distribution, Mg^{2+} content and removed Mg^{2+} (%) of Sep before and after HCl activation treatment.

Items	Sep	A-Sep-0.5M	A-Sep-1.0M	A-Sep-1.5M	A-Sep-2.0M	A-Sep-2.5M
BET surface area (m^2/g)	81.23	174.37	184.57	219.95	239.43	217.56
Total pore volume (cm^3/g)	0.0947	0.1515	0.1662	0.1902	0.2055	0.1844
0-4.3 nm Pore volume (cm^3/g)	0.0331	0.0794	0.0898	0.1048	0.1100	0.0927
4.3-9.3 nm Pore volume (cm^3/g)	0.0171	0.0220	0.0240	0.0267	0.0303	0.0284
9.3-23.7 nm Pore volume (cm^3/g)	0.0445	0.0501	0.0524	0.0587	0.0652	0.0633
Mg^{2+} content (%)	11.16	10.54	9.92	6.46	6.19	5.89
Removed Mg^{2+} (%)	–	5.56	11.12	42.11	44.53	47.22

As shown in Fig. 3a, the meso-porous structures inside Sep particles are determined by the similar N_2 adsorption-desorption isotherm curves of Sep and A-Sep particles, which are classified as H3 hysteresis loops and related to the capillary condensation of filled and emptied meso-pores [51]. After acid activation treatment, the amount of adsorbed N_2 increases significantly, indicating an increased number of meso- and micro-pores inside the A-Sep. This was further confirmed by the results shown in Fig. 3b and Table 1, where the meso- and micro-pore volumes of A-Sep samples increase sharply compared to the original Sep sample. This results in a significant increase in specific surface area, e.g., up to 1.2-2.0 times of A-Sep samples compared to 81.23 m^2/g of Sep. Obviously, the increased numbers of meso- and micro-pores result in an increase of specific surface area, which is also shown in Table 1.

It should be noted that the condition of the acid treatment must be precisely controlled since A-Sep fibrous particles with expended internal channels but not collapsed structures are desired. With regard to the items of the BET specific surface area and the total pore volume as well as the specified range of pore sized volume, all results show a first increasing trend, followed by a decrease with elevated HCl concentration and a peak value at sample A-Sep-2.0M. The acid activation treatment with excessively high acid concentration might cause a collapse of the Sep structure [53]. Therefore, the decreased values of the BET specific surface area and total pore volume from the samples treated by HCl above 2.0 M HCl indicate the partial collapse of Sep structures. In addition, the significantly increased total pore volume is

predominantly caused by a notable increase of very small pores with size < 4.3 nm and an evident increase of 4.3-9.3 nm and 9.3-23.7 nm of pore volume. This indicates that acid activation treatment is more beneficial to increase the micro- and meso-pore levels, which should be attributed to the replacement of Mg^{2+} by H^{+} [54]. As a result, 2.0 M HCl is the ideal concentration for acid activation treatment and the sample A-Sep-2.0M was chosen for the following sulfonation treatment.

3.1.2 Surface modification of Sep particles

Achieving a uniform dispersion of inorganic nanoparticles in a polymer matrix is challenging and also essential to obtain improved properties of nanocomposites. Silane coupling agents are classically used to functionalize inorganic nanoparticles by introducing an organic group via covalent bonding to the surface of mineral fillers [55]. The silane coupling agent TPES was used in this study to improve the compatibility of Sep inorganic particles with the ABPBI polymer. After acid treatment, a large number of Si–OH groups could be found on the external and internal surfaces of Sep particles, which was beneficial for the grafting of PTES by a silanol condensation reaction as illustrated in Fig. 5. Through a further sulfonation process, the sulfonated benzene rings on the surface of Sep particles could link with basic Im groups in ABPBI chains by ionic bonds, thus promoting the compatibility between S-Sep and ABPBI. The sulfonation degree was determined via titration measurement, while the changes of hydrophilicities and chemical structures before and after surface modification were measured by changes of contact angle (CA) and FTIR spectra.

Through the same process of sulfonation and sulfonation degree measurement, the concentration of $–SO_3H$ groups grafted onto the surface of S-Sep particles was found to be 0.09 mmol/g, which was less than the 0.13 mmol/g reported by Beauger et al. [34]. This can be attributed to differences in the employed raw materials. The BET specific surface area of Sep particles in this study was 239 m^2/g (sample A-Sep-2.0M in Table 1), while Beauger et al. employed 320 m^2/g [34].

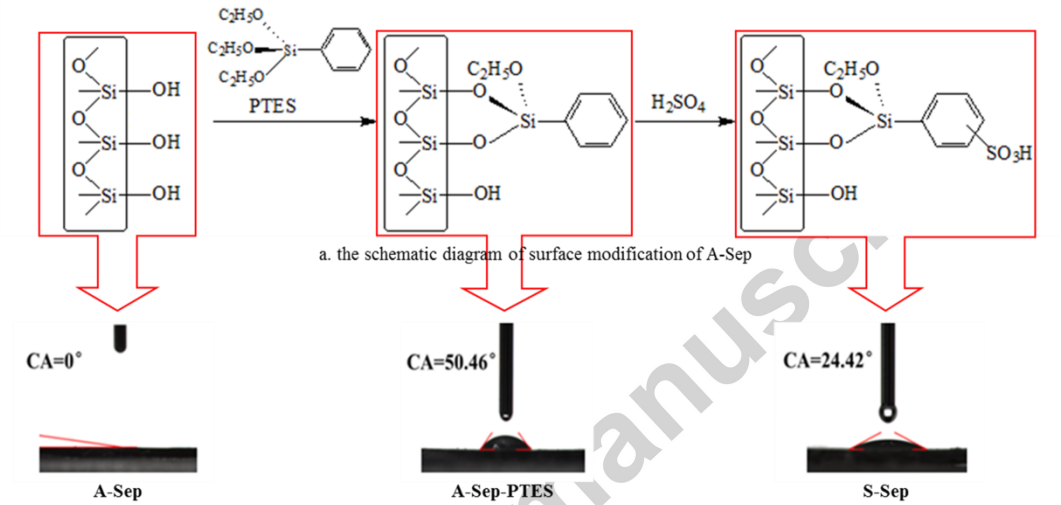

b. CA results of deonized water on particles of A-Sep, A-Sep-PTES and S-Sep

Fig. 4 Schematic diagram of surface modification of A-Sep (a) and CA results of deionized water on A-Sep, A-Sep-PTES and S-Sep particles (b).

Fig. 4a shows the complete process of surface modification and Fig. 4b displays the results of CA of deionized water of samples A-Sep, A-Sep-PTES, and S-Sep, e.g. 0°, 50.46°, and 24.42°, respectively. The CA of 0° from A-Sep indicates its high hydrophilicity due to the large number of Si–OH on the surface after acid treatment. After grafting with PTES, the Si–OH group on the surface of the A-Sep was partially replaced by hydrophobic phenyl groups according to the condensation reactions between Si–OH and $Si–OC_2H_5$. This led to a greatly increased CA from A-Sep-PTES. After further sulfonation, the hydrophilic $–SO_3H$ groups grafted into hydrophobic phenyl rings evidently improved the hydrophilicity of S-Sep.

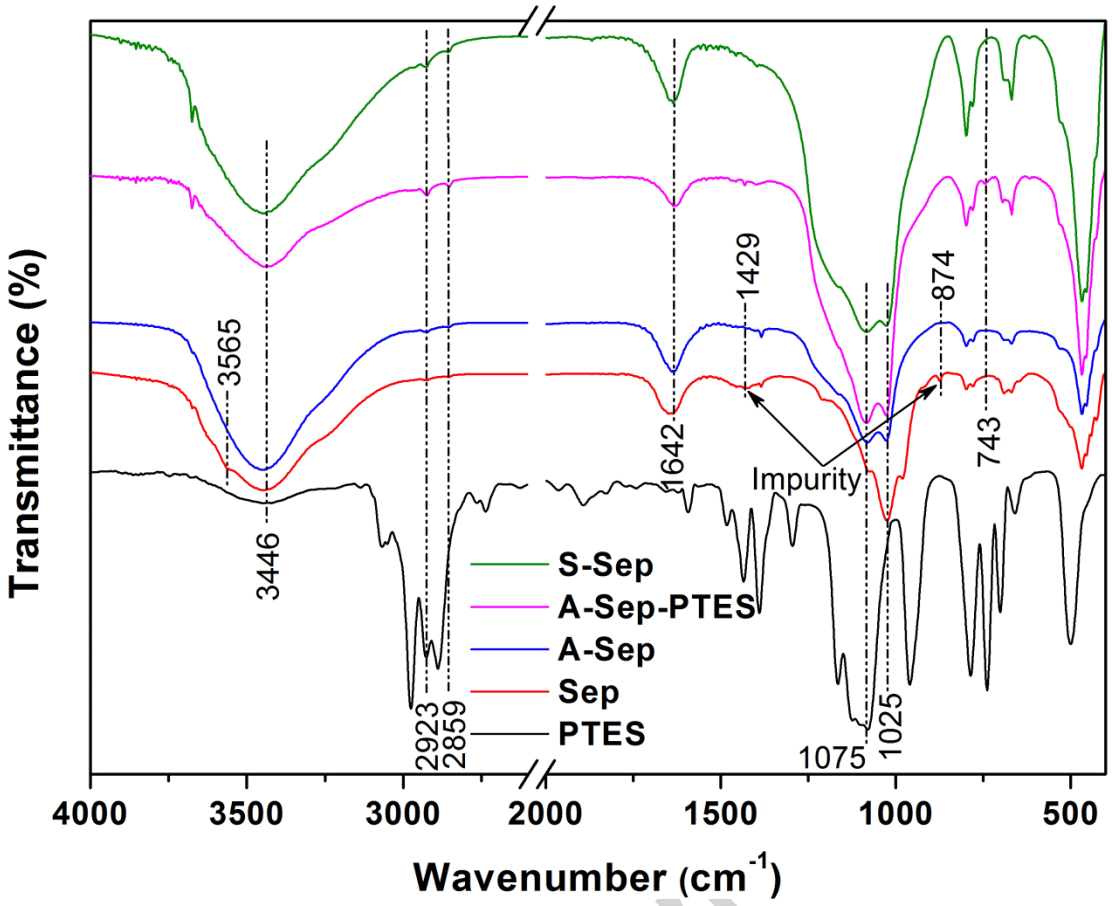

Fig. 5 FTIR spectra of PTES, A-Sep-2.0M, A-Sep-PTES, and S-Sep particles.

The chemical structures that changed via acid activation and surface modification were investigated via FTIR. With regard to the spectrum of Sep, the O–H stretching vibration from Mg_3OH in the internal tunnels of Sep (Fig. 1B) appeared at 3565 cm^{-1}. The bands at 3446 and 1642 cm^{-1} correspond to the stretching and deformation vibration modes of O–H from Si–OH in Sep and bound water molecules [56], while the bands at 1075 and 1025 cm^{-1} could be assigned to the vibration modes of Si–O(H) groups and Si–O–Si chains [52], respectively. Asymmetric and symmetric stretching modes found at 1429 and 874 cm^{-1} could be attributed to $(CO_3)^{2-}$, which confirms the presence of carbonate impurities [57]. In comparison, the characteristic peaks at 3565, 1429, and 874 cm^{-1} become invisible in the spectrum of A-Sep-2.0M,

indicating successful effects of magnesium and impurity removal through the acid activation treatment of 2.0 M HCl [57]. Furthermore, compared to original Sep, the clearly increased intensities of peaks at 3446 and 1642 cm^{-1} in the spectrum of A-Sep-2.0M indicate an increase of –OH from Si–OH. Through acid activation treatment, H^+ from acid gradually replaced Mg^{2+}, resulting in the generation of more Si–OH groups (as shown in Fig. 1C).

When coupled with PTES, the characteristic peaks of C–H asymmetric and symmetric stretching vibrations at 2923 and 2859 cm^{-1} and that of the Si–C stretching vibration at 743 cm^{-1} confirmed the existence of PTES [34]. Compared to A-Sep-2.0M, the intensities of peaks at 3446 and 1642 cm^{-1} in A-Sep-PTES decreased while peaks at 1075 cm^{-1} increased. This indicates that the introduction of PTES partially consumed Si–OH groups through the silanol condensation reaction between PTES and Sep, resulting in the increased ratio of the Si–O structure [34]. After the sulfonation process, the obtained S-Sep shows a relatively similar FTIR spectrum to A-Sep-PTES in which, the increased intensities of peaks of 3446 and 1642 cm^{-1}, associated to hydroxyl, can be explained by the improved hydrophilicity because the –SO_3H group was grafted to the benzene ring. The analytical characterization of sulfonated Sep particles is not straightforward, because the concentration of the phenyl groups in sulfonated particles is low, thus limiting the use of FTIR. However, the sulfonated product showed a distinctively reduced hydrophilicity as shown in Fig. 4, indicating successful sulfonation reaction.

3.2 Properties of ABPBI/S-Sep composite membranes

Composite membranes were prepared with various amounts of modified S-Sep particles via *in-situ* synthesis with a targeted thickness of 50 μm. The structures and morphologies of the obtained membranes were characterized by XRD and SEM-EDS. Their investigated properties were mechanical properties, thermal, oxidative, and dimensional stabilities, water uptake, PA absorptivity and retention capacity, and proton conductivity. Their performance was compared to ABPBI membrane and commercial Nafion 212 as well as results from references [33, 34, 58-60].

3.2.1 XRD study

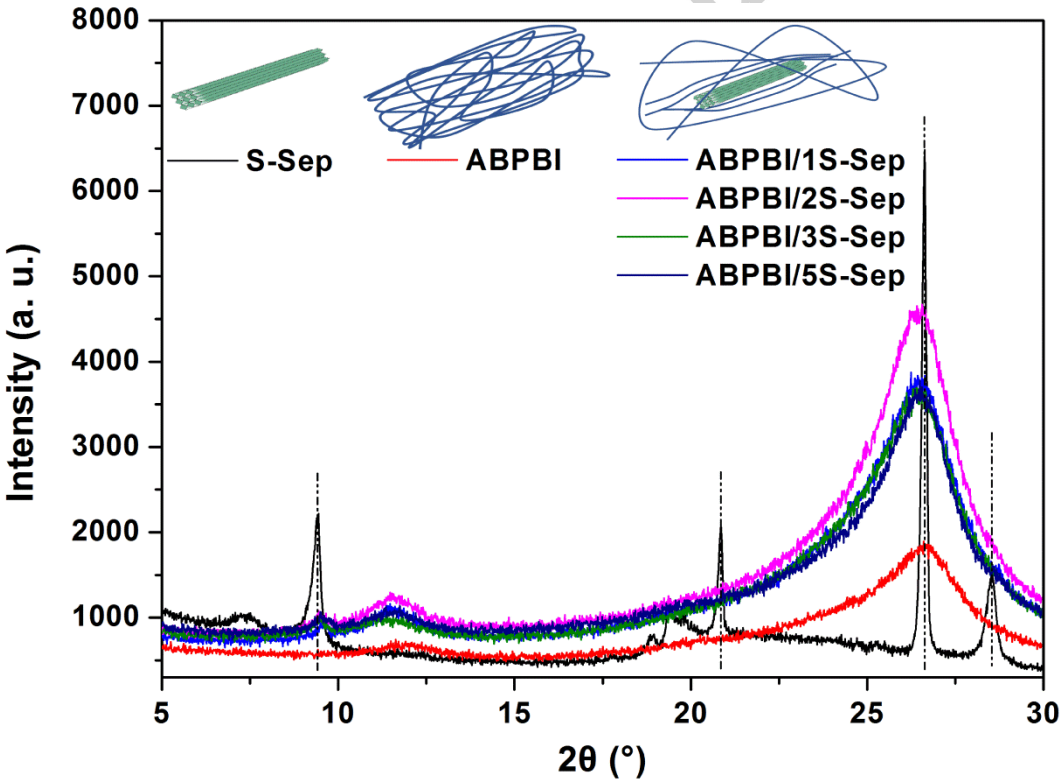

Fig. 6 XRD spectra of S-Sep particles, ABPBI, and ABPBI/S-Sep composite membranes.

The effects that Sep fibrous particles had on the crystal structure of ABPBI/S-Sep composite membranes are presented in Fig. 6. The strong diffraction

peaks at 9.45°, 20.84°, 26.64°, and 28.54° from S-Sep particles, that could be assigned to an orthorhombic crystalline system [61], indicate that the S-Sep sample maintains an ideal crystalline structure after acid activation and surface modification treatments. Two rather weak and broad peaks at 11.95° and 26.55° were found in the pattern of pristine ABPBI membrane, which correspond to a characteristic stacking of ABPBI chains, indicate its amorphous or a semi-crystalline structure [62]. In the patterns of ABPBI/S-Sep composites, the visual peak at 9.45° and the overlapping peaks at 20.84°, 26.64°, and 28.54° from Sep particles show the existence of Sep in the polymer matrix and indicate that ABPBI/S-Sep samples still maintain an amorphous or semi-crystalline structure [63]. It is worth noting that the characteristic peaks at 11.95° and 26.55° were found to increase in intensity and sharpness, which implies a crystallization tendency of the ABPBI polymer. This suggests that, with S-Sep fibrous particles being intercalated into the ABPBI chains, these are driven to stack along Sep fibers, therefore resulting in enhanced crystallinity [63, 64]. However, the excess S-Sep does not necessarily reorder polymer chains, due to the agglomeration of particles, which might explain the decreasing intensity of the peak at 26.55° that was found in the samples ABPBI/3S-Sep and ABPBI/5S-Sep.

3.3.2 FESEM-EDS analysis

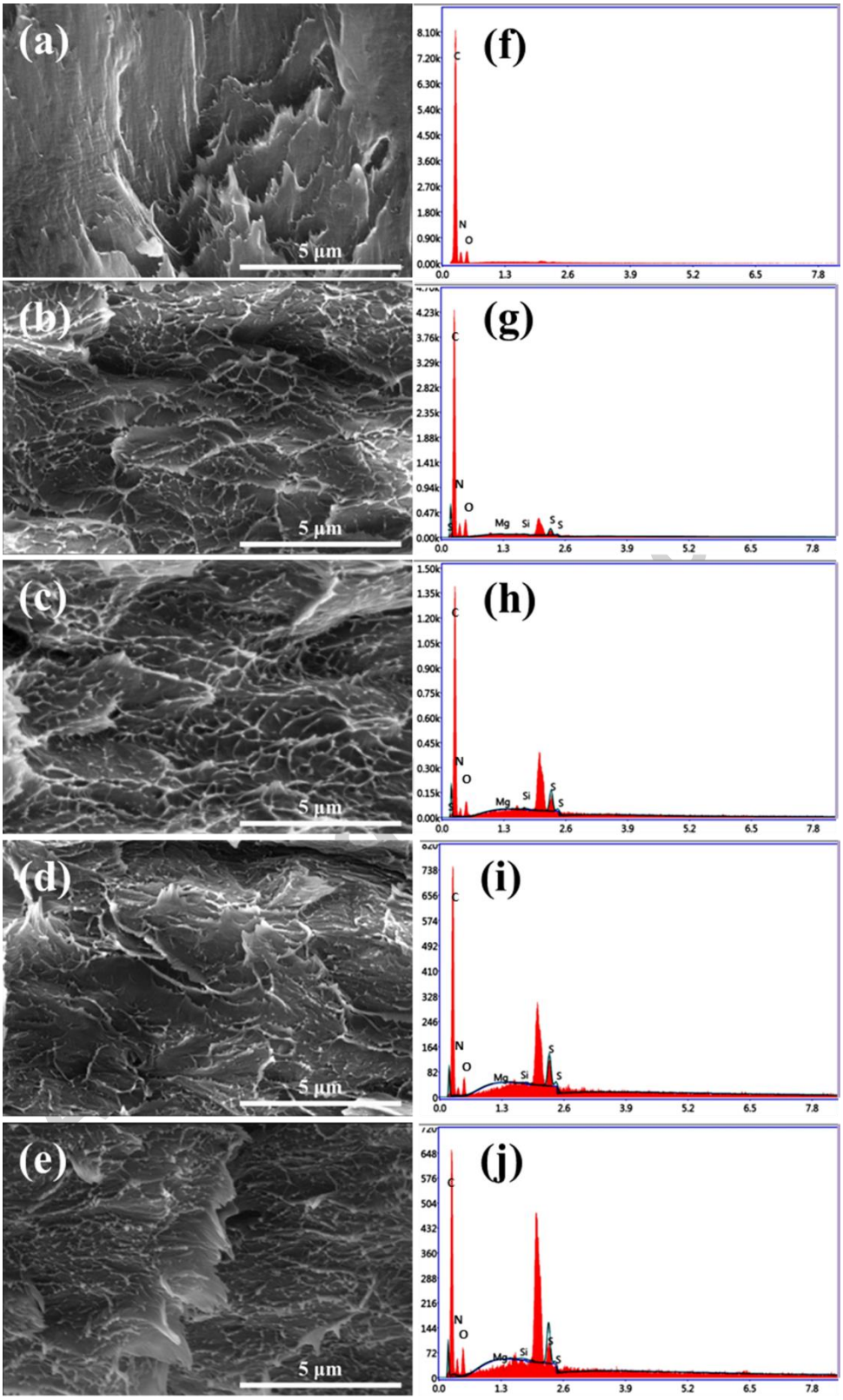

Fig. 7 SEM images of the cross-section of ABPBI (a), ABPBI/1S-Sep (b), ABPBI/2S-Sep (c), ABPBI/3S-Sep (d), ABPBI/5S-Sep (e) composite membranes, and EDS spectra of ABPBI (f), ABPBI/1S-Sep (g), ABPBI/2S-Sep (h), ABPBI/3S-Sep (i), and ABPBI/5S-Sep (j) composite membranes

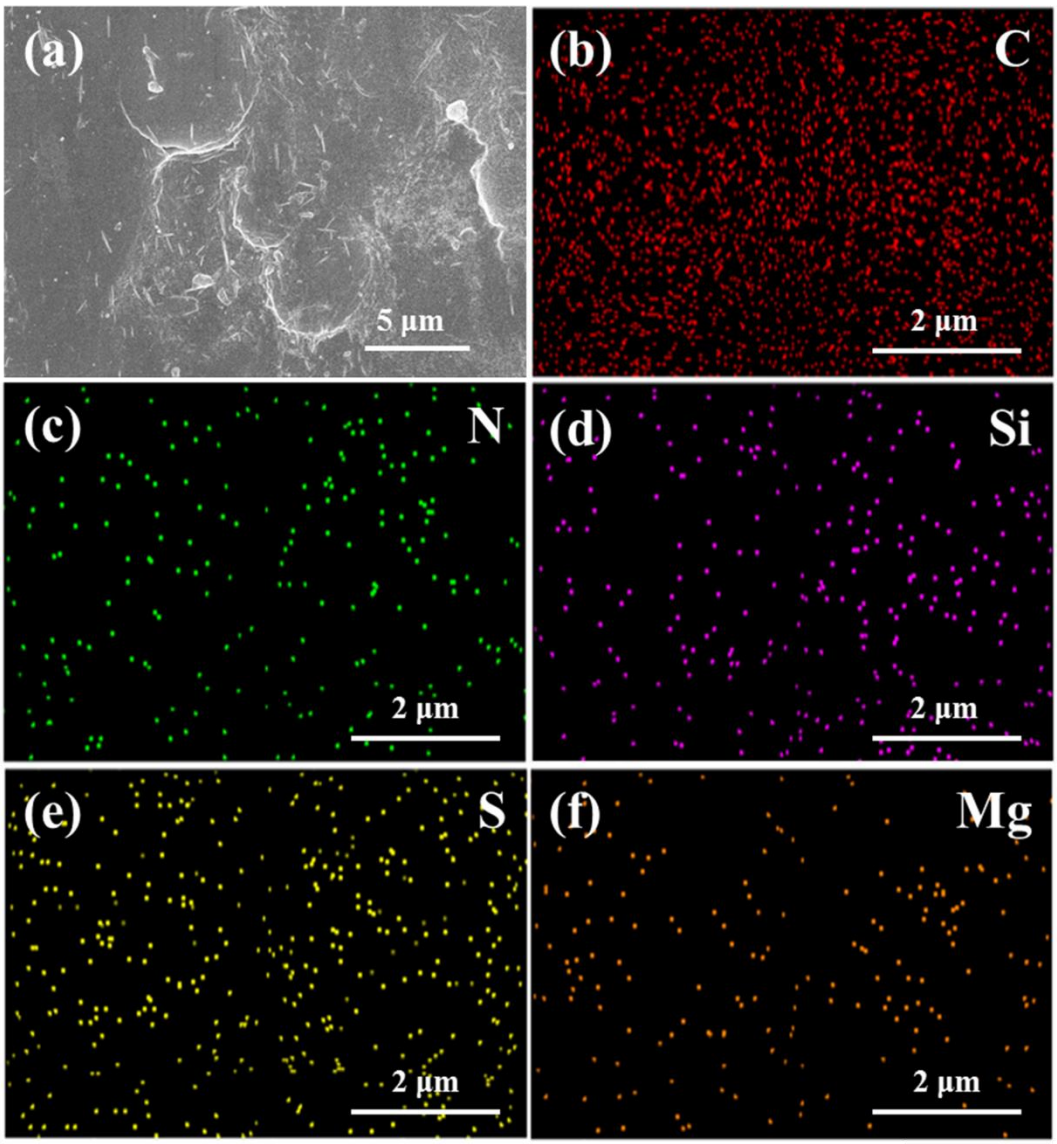

Fig. 8 Surface morphology (a) and elemental distribution mappings of C (b), N (c), Si (d), S (e), and Mg (f) in the ABPBI/2S-Sep composite membrane.

SEM images of ABPBI and ABPBI/S-Sep composite membranes are shown in Fig. 7. A typical polymer ductile fracture morphology [65] of the pristine ABPBI was observed Fig. 7a) and no other elements (except for C, N, and O) appeared in the relative EDS spectra Fig. 7f), indicating its pureness. With the introduction of Sep, the images in Fig. 7b-e display typical brittle fracture morphologies, which generally indicate good compatibility between the S-Sep particles and the ABPBI polymer. Moreover, the images in Fig. 7g-j show the characteristic peaks of the elements of

S-Sep particles, in which, the relative intensity changes of peaks agree with the increasing amount of Sep. Compared to the morphologies of the neat cross-sections shown in Fig. 7b and c, more and unevenly distributed fibrous-like morphologies can be observed due to the ductile fracture of ABPBI in Fig. 7d and e, indicating that the aggregation of Sep particles may happen when more than 2 wt.% of Sep is added [58]. To further confirm the good dispersion of S-Sep particles in the ABPBI matrix, surface morphology and element mapping of ABPBI/2S-Sep composite membranes are shown in Fig. 8. In Fig. 8a, the Sep fibrous particles are clearly visible and show good compatibility with the ABPBI matrix, while the element mapping of Si, S, and Mg in Fig. 8d-f (which only exist in S-Sep particles) confirm the uniformity of the distribution of S-Sep particles in the ABPBI matrix.

3.3.3 Dynamic mechanical properties

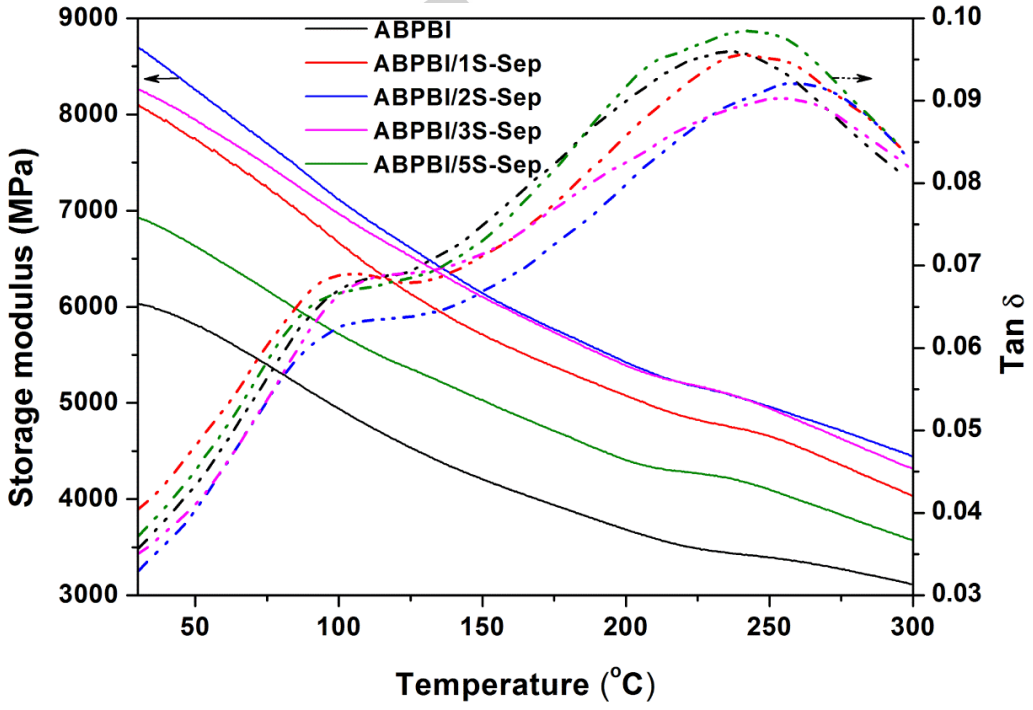

Fig. 9 Change in the storage moduli and tan δ with temperature for ABPBI and ABPBI/S-Sep composite membranes.

Table 2 Thermo-mechanical data, tensile strength and elongation at break of pristine ABPBI membrane and ABPBI/S-Sep composite membranes obtained via DMA and tensile test.

Samples	HDT (°C)	E' (GPa)				Tensile strength (MPa)	Elongation at
		25 °C	100 °C	200 °C	300 °C	at 25 °C	break (%)
ABPBI	237.8	6.0	4.9	3.7	3.1	72.4±4.8	56.4±6.9
ABPBI/1S-Sep	244.7	8.2	6.7	5.1	4.0	83.4±5.4	54.3±5.3
ABPBI/2S-Sep	256.5	8.8	7.1	5.4	4.4	99.0±5.7	44.7±6.1
ABPBI/3S-Sep	248.9	8.3	7.0	5.4	4.3	90.0±6.5	46.2±5.4
ABPBI/5S-Sep	241.5	6.9	5.7	4.4	3.6	81.1±6.2	41.5±7.3

The mechanical properties of the membranes are important because they ultimately affect the durability of a PEMFC within the operating temperature range. The effects of Sep fillers on the mechanical properties of the composite membranes were investigated by DMA within a range from room temperature (25 °C) to 300 °C and tensile tests were conducted at 25 °C. The temperature-dependence of the storage moduli as well as tan δ of ABPBI and ABPBI/S-Sep composite membranes are shown in Fig. 9. The heat deflection temperature (HDT) values according to the peak of tan δ curves in Fig. 9, and the storage moduli (E') at 25, 100, 200, and 300 °C as well as the results for tensile strength at room temperature are summarized in Table 2. The values of HDT, E', and tensile strengths of composite membranes are universally higher compared to virgin ABPBI membranes regardless of the temperature and within a range from 25 to 300 °C. In heterogeneous systems, the mechanical properties of polymer composites generally depend on the dispersion of the secondary phase. On the one hand, a nano-scaled dispersion of the secondary component can improve the mechanical properties by reducing the mobility of polymer chains, which leads to a stiffer material [32]. Micro-scaled dispersion, especially resulting from aggregation, can lead to a negative effect on the mechanical properties by causing discontinuities in

the polymer phase [66]. In combination with previous SEM results, the greatly improved mechanical properties of composite membranes shown in Fig. 9 and Table 2 are caused by the good dispersion of S-Sep particles in the ABPBI matrix.

T_g is the temperature of the primary phase transition or the temperature when whole polymer chain motion occurs, and the T_g value of ABPBI is normally above 425 °C [6, 48]. Thus, the peak of the tan δ curve in Fig. 9 presents the occurrence of the secondary transition of the ABPBI polymer or of chain segment motion. The HDT, presented as a temperature and corresponding to a tan δ curve peak in Fig. 9, reflects the ability of polymer materials to resist deformation. The increased HDT values of composite membranes shown in Table 2 compared to 237.8 °C of the original ABPBI indicate their improved ability of resist deformation, which is due to the enhanced crystallinity. Furthermore, the ABPBI/2S-Sep sample exhibits the highest value of HDT and the best mechanical properties between 25-300 °C, especially, 5.4 GPa of E' at 300 °C of the ABPBI/2S-Sep sample is close to 6.0 GPa of E' at 25 °C of ABPBI, which indicates that the ABPBI/2S-Sep composite membrane has desirable thermo-mechanical properties, indicating it as useful for wide temperature range applications.

3.3.4 Thermal stability

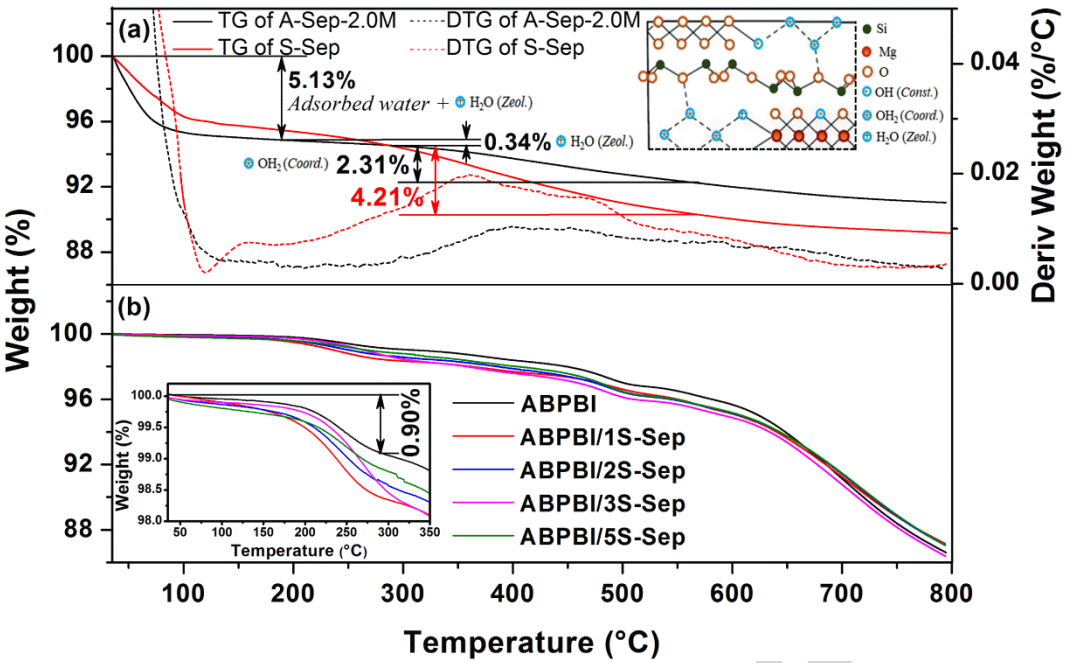

Fig. 10 TG and DTG plots of A-Sep-2.0M and S-Sep (a), as well as TG plots of ABPBI and ABPBI/S-Sep composite membranes.

The thermal stabilities of A-Sep-2.0M and S-Sep particles as well as those of ABPBI and ABPBI/S-Sep composite membranes are presented in Fig. 10. Sep particles generally contain water in four forms: physically adsorbed water, zeolitic water, coordinated water, and constitution water [67], which is also shown in Fig. 10a. The exception is constitution water which will be removed above 810 °C due to dehydroxylation. After sulfonation modification, the weight loss of S-Sep below 190 °C is slightly lower than that of A-Sep-2.0M due to the moderate decline of hydrophilicity, which agrees with the CA results shown in Fig. 4. The weight loss above 290 °C includes the release of decomposed organic groups from S-Sep particles with the exception of the release of both coordinated water and constitution water. Between 290 and 570 °C, the weight loss of A-Sep-2.0M is 2.31%, while that

of S-Sep is 4.21%. The difference of 1.90% can be ascribed to the grafted organic –SO_3H groups. As a result, the 1.90% weight loss due to the organic groups release is equivalent to a sulfonation degree of 0.08 mmol/g, which is consistent with the result of 0.09 mmol/g determined via titration test.

ABPBI is hydroscopic and thermally stable, and the weight loss below ≈ 470 °C is caused by the volatilization of H-bonded water and the thermal oxidation decomposition of ABPBI oligomers [48, 68]. Therefore, the higher weight loss (about 0.25 to 0.71 wt.%) of ABPBI/S-Sep compared to that of pristine ABPBI below 290 °C is mainly a result of free and bonded water, indicating that ABPBI/S-Sep composite membranes have sufficient thermal stability for their application in HT-PEMFC (up to 200 °C).

3.3.5 Oxidative stability

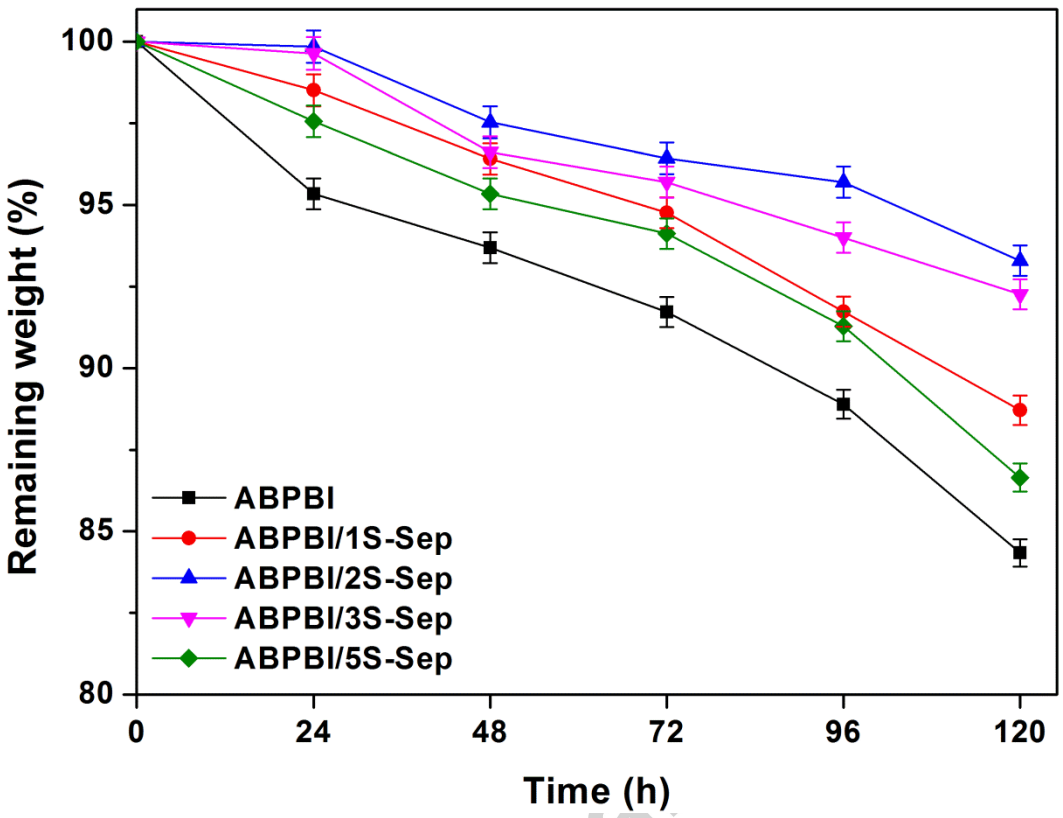

Fig. 11 Oxidative stability plots of ABPBI and ABPBI/S-Sep composite membranes.

In addition to the thermo-mechanical stability of the membranes, their oxidative stability is also an important parameter to evaluate the long-term durability of a PEMFC. During the run-time of the cell, the H_2O_2 formed by oxygen cross-over from cathode to anode reacts with hydrogen and can degrade to ·OH and ·OOH radicals, which subsequently attack the C–H bonds of the polymer, thus resulting in degradation of the polymer matrix [49]. Oxidative stability plots of ABPBI and ABPBI/S-Sep composite membranes are shown in Fig. 11. All ABPBI/S-Sep composite membranes show a significant improvement in oxidative stability compared to pristine ABPBI. Furthermore, the oxidative stability from ABPBI/2S-Sep is superior to PBI-clay composite membranes according to published

results [47, 49, 50, 69]. This advantage can be attributed to the unique structure of composites. As discussed before, ABPBI chains are stacked along Sep fibers, thus showing enhanced crystallinity. This structure with a tight polymer chain stack effectively hinders free radicals from attacking ABPBI chains, thus postponing the development of oxidation degradation. Furthermore, uniformly dispersed Sep are involved in H-bonding interactions with ABPBI chains; as a result, these H-bonds shield the polar groups of ABPBI from attack by the free radicals [69].

3.3.6 Water uptake, phosphoric acid doping level, and retention ability

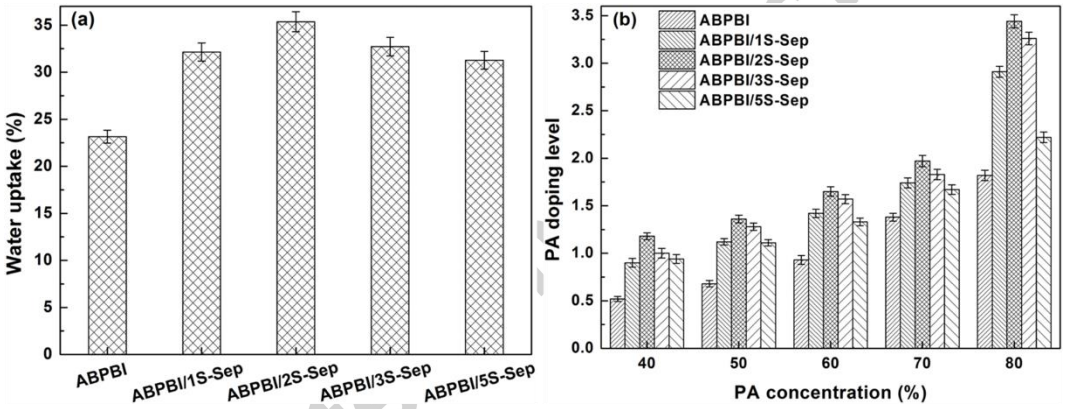

Fig. 12 WUs under saturated humidity (a) and PA DLs (b) of ABPBI and ABPBI/S-Sep composite membranes.

The water absorbability can indirectly reflect the proton transfer property of a PEM and is therefore a key index since water molecules have a key role in conducting protons in ABPBI/S-Sep composite membranes with low PA DLs. The water uptake (WU) values of pristine ABPBI and ABPBI/S-Sep composite membranes at atmospheric conditions are shown in Fig. 12a. Due to Im group H-bonding H_2O [48], the pristine ABPBI membrane shows a WU of 23.15%. With the incorporation of S-Sep particles, the WU of ABPBI/1S-Sep, ABPBI/2S-Sep, ABPBI/3S-Sep, and ABPBI/5S-Sep composite membranes are 32.15, 35.36, 32.72, and 31.26%,

respectively. The WU of composite membranes are much higher than that of pristine ABPBI and present a first increasing tendency, followed by a decrease with increasing S-Sep content. The hygroscopic nature of Sep particles and the presence of hydrophilic $–SO_3H$ groups on the surface of S-Sep favor the increased WU; however, the aggregation of S-Sep particles which occurs in ABPBI/3S-Sep and ABPBI/5S-Sep are likely responsible for the decreased tendency of the WU when the content of S-Sep exceeds 2 wt.%.

For normal PA-PBI membranes with high PA DLs, it is essential to evaluate the PA retention ability since it suffers from problems such as free PA leaching at hydrous condition and degradation above 180 °C as mentioned above. In this study, though all composite membranes for the proton conduction measurements had free PA removed by repeatedly boiled in deionized water, it is still important to disclose the capacity and pattern of PA absorbance and retention through PA doping and retention tests.

The PA DLs of the ABPBI and ABPBI/S-Sep composite membranes are shown in Fig. 12b. The DLs of ABPBI and ABPBI/S-Sep composite membranes increase with increasing PA concentrations, and show the same trend as the WU of membranes with different S-Sep proportions. For the pure ABPBI membrane, the Im group on the ABPBI itself can be ion-bonded with acidic phosphate molecules, resulting in an increased PA DL [48]. With the incorporation of S-Sep into composite membranes, the abundant Si–OH groups that exist in both external and internal surfaces of S-Sep can absorb PA molecules via H-bonds. Extended internal channels

might trap some PA molecules, thus resulting in remarkably higher PA DLs. Nevertheless, the decreased PA DLs of composite membranes with increasing S-Sep content from 3 to 5 wt.% are caused by the aggregation of S-Sep particles, which reduce the amount of exposed Si–OH groups and pore volumes of S-Sep particles.

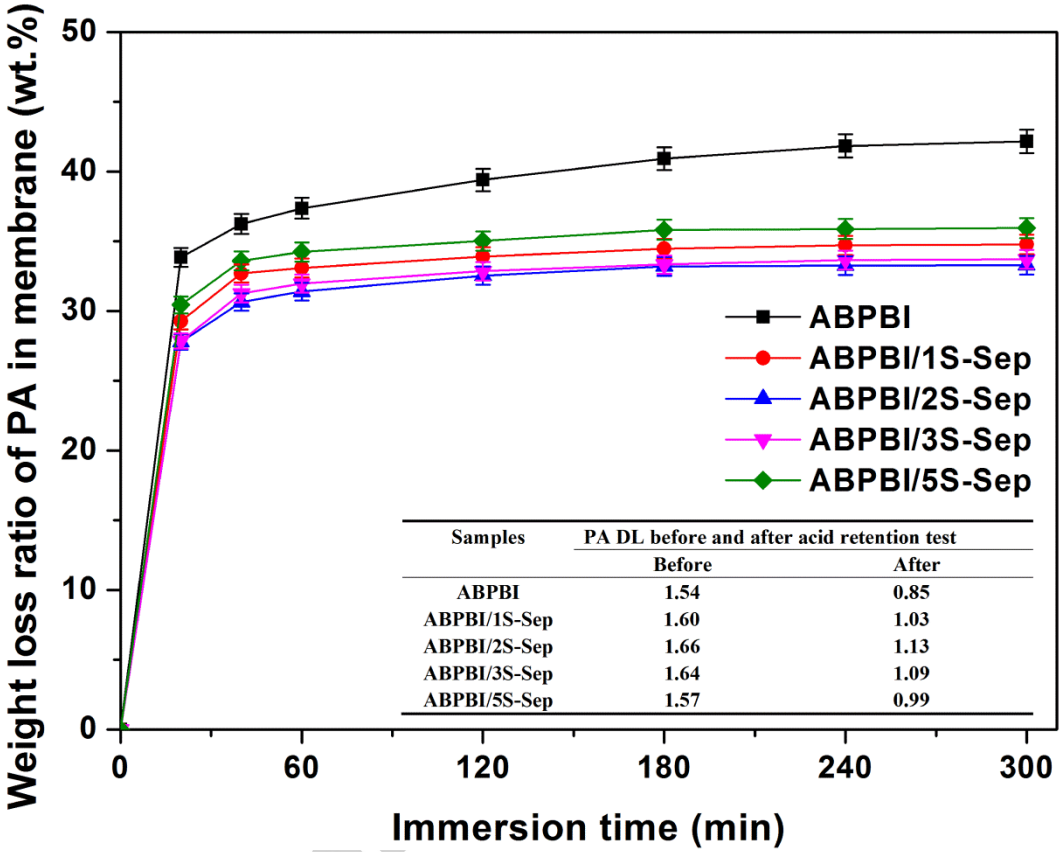

Samples	PA DL before and after acid retention test	
	Before	After
ABPBI	1.54	0.85
ABPBI/1S-Sep	1.60	1.03
ABPBI/2S-Sep	1.66	1.13
ABPBI/3S-Sep	1.64	1.09
ABPBI/5S-Sep	1.57	0.99

Fig. 13 Time dependence of the weight loss ratio of PA in ABPBI and ABPBI/S-Sep composite membranes.

An acid leaching test following a previously reported method [49, 69] was conducted to characterize the acid retention ability of PA doped membranes. To investigate the PA leaching behavior, membrane samples were chosen with similar PA DLs. The PA retention ability of a membrane can be calculated by counting the weight loss ratio and the obtained results are plotted in Fig. 13. Two states of PA exist in a membrane, e.g. free PA (in free mobility) and bound PA (in restricted mobility), in which, free PA can be mostly removed through water flashing for a sufficiently

long period of time, while the bounded PA cannot be removed [49]. Fig. 13 shows that all membranes display two distinct periods of PA loss rate: a fast loss period, which roughly happens during the first 0.5 h, corresponding to the release of PA in free mobility in the shadow surface. This period is followed by a slow loss in the deep layer. Furthermore, the PA loss rate and loss ratio in the ABPBI membrane are faster and heavier than in composite membranes, and the most enhanced PA retention ability was obtained for the ABPBI/2S-Sep sample with 33.3 wt.% of loss ratio compared to that of ABPBI with 42.2 wt.%. Firstly, due to the barriers from more regular arrangement of ABPBI chains, the composite membranes show a slower loss rate. Secondly, due to the H-bonding reactions between PA and ABPBI, PA and Si-OH as well as the oxygen on silicate layers [49], result in PA in restricted mobility [70]. Therefore, the composite membranes have a better PA retention ability, obviously benefitting from Sep particles with enlarged surface area and better dispersion in the ABPBI matrix.

3.3.7 Dimensional stability

Table 3 Swelling ratios of area and volume of PA doped ABPBI and ABPBI/S-Sep composite membranes.

Samples	Swelling ratio (%)	
	Area	Volume
ABPBI-1.66PA	27.80±1.4	132.76±3.9
ABPBI/1S-Sep-1.74PA	20.70±1.2	93.66±2.8
ABPBI/2S-Sep-1.92PA	18.01±1.1	78.97±2.3
ABPBI/3S-Sep-1.83PA	20.90±1.2	98.97±2.9
ABPBI/5S-Sep-1.67PA	22.57±1.3	110.70±3.2

During a PEMFC operation, the PA-PBI PEM undergoes changes in its dimensions which can affect the fabrication of MEA as well as the proton conduction

kinetics and fuel cell performance [49]. The swelling ratio of area (ΔS) and volume (ΔV) of both ABPBI and ABPBI/S-Sep composite membranes with similar PA DLs are listed in Table 3. ΔS and ΔV of PA doped composite membranes are lower than that of PA-ABPBI and the sample ABPBI/2S-Sep shows the best dimensional stability. Furthermore, the results of ΔS and ΔV from ABPBI/S-Sep composite membranes are much better than that of the PBI-clay composite membranes reported previously [32]. Generally, in a PA-PBI membrane, the dimensional change is governed by PA loss since the PBI polymer with all aromatic main chains is highly rigid. Therefore, the 27.80% of ΔS and 132.76% of ΔV from ABPBI-1.66PA are mainly due to the leaching of free PA. To achieve a PEM with improved dimensional stability, acid-base blending via crosslinks between acid and based phases is an effective way [71]. In fact, an ABPBI membrane with very low PA DL (e.g. less than 1) is dimensional stable because the PA molecules act as a crosslinker. As a result, the significantly improved dimensional stability of ABPBI/S-Sep can be ascribed to ionic bonds between $-SO_3$, which has been grafted onto Sep particles and basic Im groups in ABPBI chains as well as the increased crystallinity of ABPBI polymers.

3.3.8 Proton conductivity

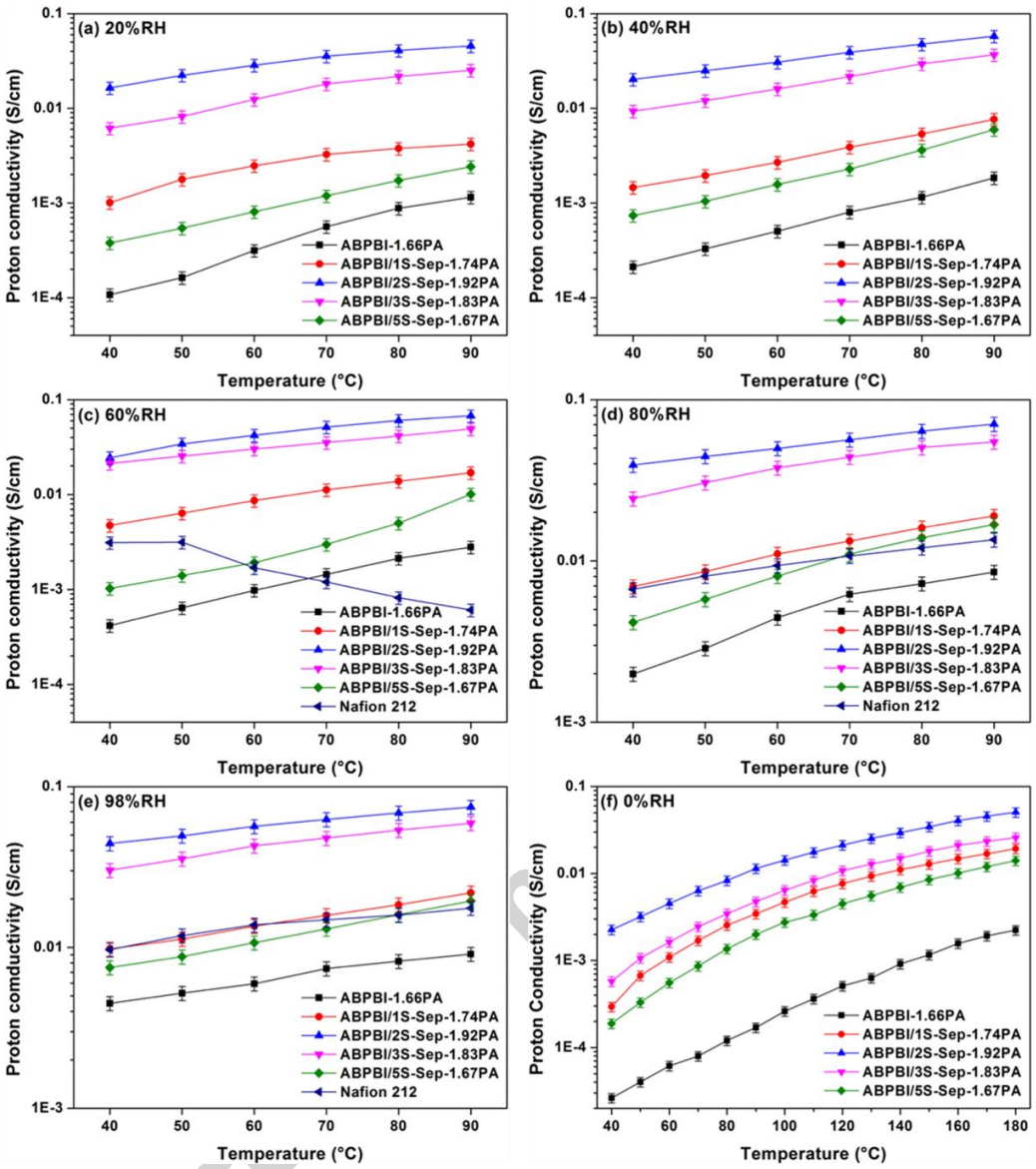

Fig. 14 Proton conductivities of PA doped ABPBI and ABPBI/S-Sep composite membranes at low temperature from 40 to 90 °C under 20% RH (a), 40% RH (b), 60% RH (c), 80% RH (d), 98% RH (e), and at a broad temperature range from 40 to 180 °C under 0% RH (f).

Table 4 Thickness and E_a of PA doped ABPBI and ABPBI/S-Sep composite membranes.

Samples	Thickness	E_a (kJ/mol) in the temperature range of 40-90 °C					
	(μm)	0% RH	20% RH	40% RH	60% RH	80% RH	98% RH
ABPBI-1.66PA	67	38.73	37.57	35.08	32.58	28.27	18.13
ABPBI/1S-Sep-1.74PA	56	32.19	29.27	26.44	23.78	19.21	14.54
ABPBI/2S-Sep-1.92PA	54	26.28	23.94	19.37	15.71	11.14	9.98
ABPBI/3S-Sep-1.83PA	58	30.75	27.10	23.45	19.04	15.55	12.72
ABPBI/5S-Sep-1.67PA	62	35.64	35.09	32.67	27.19	24.61	16.79
Nafion 212	50	–	–	–	–	13.22	10.73

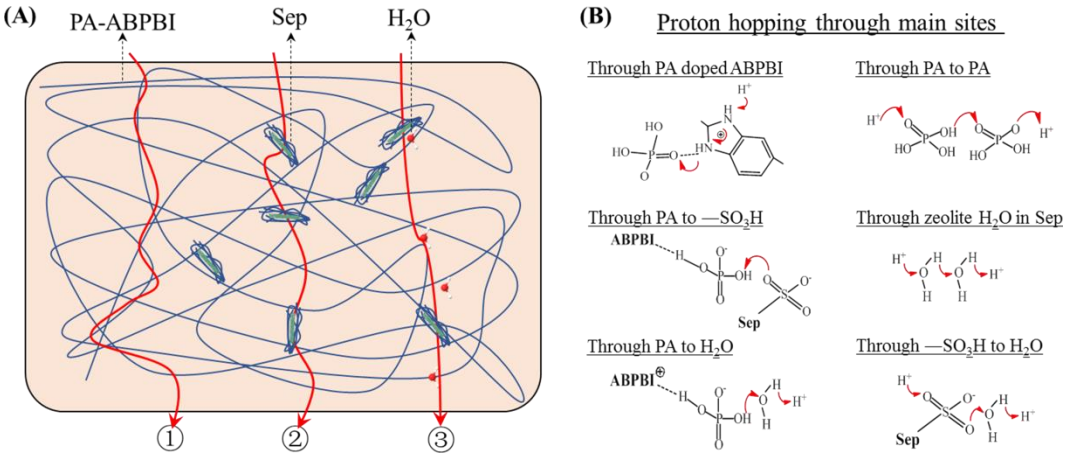

Fig. 15 Schematic diagram of proton conduction pathway (A) and main hopping sites (B) in PA doped ABPBI/S-Sep composite membranes.

Table 5 Proton conductivities of PA doped PBIs-based composite membranes.

Type of membrane	T (°C)	RH (%)	Proton conductivity (S/cm)	Reference
ABPBI/2S-Sep-1.92PA	90	20	0.046	This work
ABPBI/2S-Sep-1.92PA	90	98	0.075	This work
ABPBI/2S-Sep-1.92PA	180	0	0.051	This work
PBI/SA-SNP-15	90	95	0.032	[72]
PBI/SA-SNP-10	150	0	0.004	[72]
dABPBI-10MS	140	1	0.035	[59]
dABPBI-5MIL	150	0	0.067	[65]
Al-Si(12%)/PBI-4.75PA	150	0	0.031	[58]
PBI/IMSA-1-7.8PA	160	0	0.007	[73]
PBI-0.3%MWNT-Im	160	0	0.043	[74]
6-c-sTiO_2-PBI-OO	160	5	0.098	[60]
PBI/NP-20%	180	0	0.061	[50]
PBI-TGIC(10%)/SPAN(40%)	180	0	0.020	[20]
PBI-TGIC(10%)/SPAN(40%)	180	50	0.071	[20]
PBI+LI3-NaY_3%wt	200	0	0.054	[75]
PBI/15% Clay N, ADL 8.9	120	20	0.084	[32]
PBI/15% Clay N, ADL 8.9	150	12	0.072	[32]
PBI/15% Clay N, ADL 8.9	180	10	0.080	[32]

Since the proton conductivity of the membrane is a key parameter for estimating PEM performance, ABPBI/S-Sep composite membranes are expected to have advanced proton conductivity. To investigate the contribution of S-Sep on the proton conductivity in composite membranes, all membranes with similar PA DLs (e.g. 1.66-1.92) were investigated. The composite membranes were obtained through the steps of free PA removal (i.e., boiling in deionized water for 3 hours and then

repeatedly rinsing with deionized water), while the ABPBI-1.66PA sample was prepared with the general way, e.g. deionized water rinsing to remove free PA on the membrane surface. Their proton conductivities under the conditions of low temperatures from 40 to 90 °C and RH from 0 to 98% RH are shown in Fig. 14a-e under a broad temperature range (40-180 °C) and anhydrous conditions shown in Fig. 14f. To gain further insight into the motional processes that cause nuclear relaxation and conductivity, it is common to construct Arrhenius plots of both temperature and conductivity [76, 77]. The results of relative E_a fitted from experimental results of proton conductivities by the Arrhenius plots are listed in Table 4. Furthermore, their performance was compared to commercial Nafion 212 at LT and several PBI-clay composite membranes that were used before [33, 34, 58-60].

Fig. 14 shows that the proton conductivities of PA doped composite membranes are higher than that of ABPBI-1.66PA during test temperature ranges and various RH. The conductivity changes of membranes present a first increasing and then decreasing trend with increasing content of S-Sep particles, which is identical to the WU changes, clearly indicating the contribution of the bound water inside the S-Sep particles, or rather higher WU higher conductivity. In a PEMFC, protons can be conducted via the "vehicle mechanism" by portable species (e.g. H_3O^+, $H_5O_2^+$, etc.) in hydrous conditions and via the "Grotthuss mechanism" by fixed species (e.g. solid water molecules, pendent or ionic bonding $–SO_3H$, $–H_2PO_4$, etc.) in anhydrous conditions [70]. For PA doped PBIs and their composite membranes applied in HT-PEMFC, the proton conducting through the fixed species as both proton acceptor and donor (so-called "hopping" site) including Im group in PBIs chains, doped PA, H_2O in inorganic-organic hybrid composite membranes, and the $–SO_3H$ group in acid-base mixture membranes, have been proposed before [59].

In this study, all the above-mentioned species are involved in the reaction and the possible proton conducting paths as well as proton "hopping" sites are shown in Fig. 15A and B, respectively. Considering the similar PA DL, the significantly improved proton conductivities at various RH from ABPBI/S-Sep composite membranes will likely benefit from the introduction of S-Sep particles. As mentioned above, the H_2O found in the nano-channels of S-Sep fibrous particles is providing a continuous proton conducting path. Moreover, the joints between polymer matrix and inorganic S-Sep are likely composed of H-bonding links between PA and $–SO_3H$ as well as between PA and Si–OH. Therefore, protons are likely passing through S-Sep with a continuous route in ABPBI/S-Sep composite membranes. E_a represents the sum of the enthalpies of defect pair (charge carrier) formation and defect migration, which indicates the ease for proton hopping and rotation of both donor and acceptor. A larger value of E_a indicates that higher enthalpy is required for the proton transfer, causing lower conductivity. It has previously been reported [6] that the proton transfer through H_2O, ionic-, or H-bonds is more effective than through PA-Im link in PA-PBI membranes due to the lower E_a of proton migration. As a result, compared to simply moving through the PA—ABPBI—PA path in a PA-ABPBI membrane (path ① in Fig. 15A), the proton conducting path in ABPBI/S-Sep composite membranes was shortened through ABPBI—PA—S-Sep in the presence of S-Sep particles (path ② in Fig. 15A). The superiority from the introduction of S-Sep is evidently confirmed by the decreased E_a values measured at an anhydrous condition as shown in Table 4, e.g. 32.16 kJ/mol of ABPBI/1S-Sep-1.74PA and 26.28 kJ/mol of ABPBI/2S-Sep-1.92PA compared to 38.73 kJ/mol of ABPBI-1.66PA. Furthermore, the subsequently increased E_a values of ABPBI/3S-Sep-1.83PA and ABPBI/5S-Sep-1.67PA should be attributed to the lower amount of path ②due to S-Sep aggregation. Moreover, E_a

values of all membranes decrease with an elevated RH, which indicates that movable H_2O must participate in the proton transfer, thus resulting in a further shortened path (path ③ in Fig. 15A). The reduction of E_a from PA doped ABPBI/S-Sep composite membranes compared to the ABPBI membrane indicates that the enthalpy required for proton transfer through the composite membranes is lower. In other words, the shortened proton conduction pathways in ABPBI/S-Sep composite membranes require lower enthalpy, thus contributing excellent performance of proton conduction at a wide temperature range.

It is worth noting that, among these membranes, ABPBI/2S-Sep-1.92PA showed the highest conductivity in all conditions, reaching values above 0.01 S/cm of proton conductivities at low temperature (40-90 °C) and various RH (20-98% RH) as well as the highest measured value of 0.051 S/cm at 180 °C and 0% RH. This performance is not only superior to that of Nafion 212 at low temperatures with various RH, but also competitive to that of PBI-inorganic composite membranes with high PA DLs at high temperatures (Table 5). Compared to the above-mentioned proton conductivities of PBI-based membrane and Nafion-based membrane at low temperatures (< 90 °C) and high temperatures (> 90 °C), respectively, the ABPBI/S-Sep composite membrane is applicable in a wide temperature range.

3.3.9 PEMFC performance

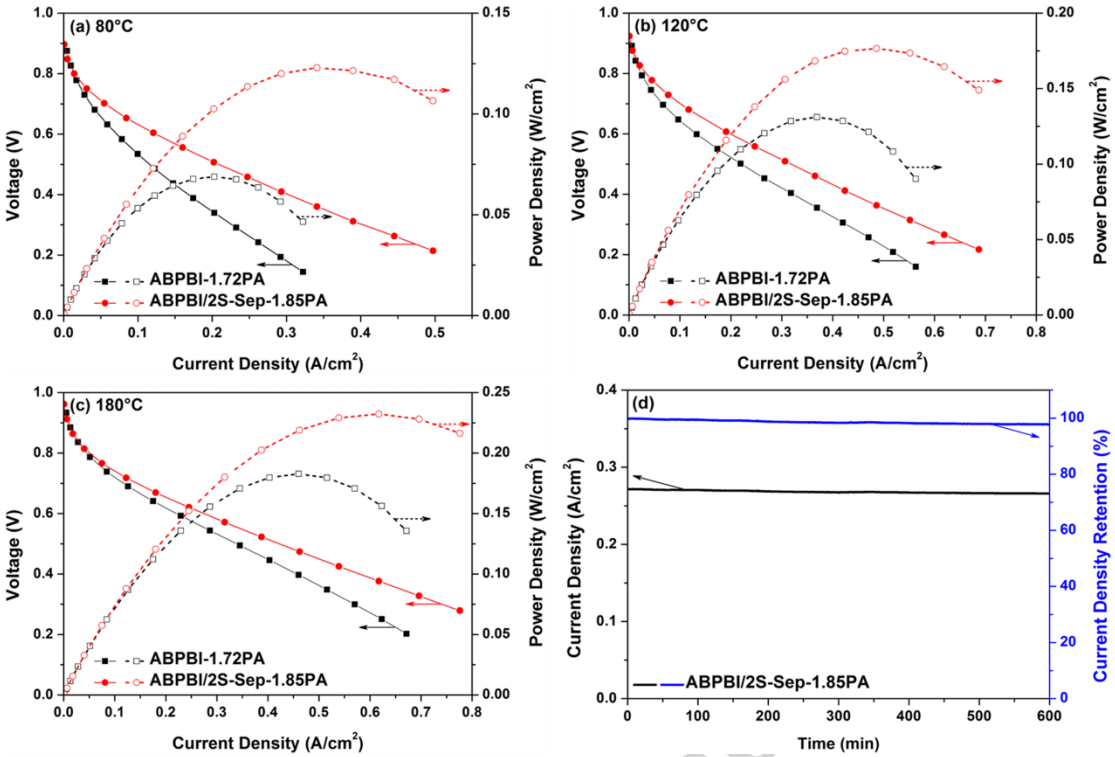

Fig. 16 Polarization and power density curves of fuel cells based on the ABPBI and ABPBI/2S-Sep composite membrane operated at 80 °C (a), 120 °C (b) and 180 °C (c) under anhydrous condition with dry H_2/O_2 at atmospheric pressure and time evolution (d) of the cell current density at a constant voltage load of 0.6 V for the MEA based on the ABPBI/2S-Sep composite membrane at 180 °C. The thickness of ABPBI and ABPBI/2S-Sep composite membrane is 64 and 52 μm, respectively.

ABPBI/2S-Sep composite membrane was chosen to test single cell properties due to its best performances and ABPBI membrane as reference. The polarization and power density curves obtained at various temperatures are shown in Fig. 16. The open circuit voltage (OCV) values of all ABPBI/2S-Sep composite membrane at 80, 120, and 180 °C are more than 0.90 V and higher than that of pure ABPBI membrane, indicating that the composite membrane is more pore-free and exhibits lower gas crossover property [78]. As can be seen in Fig. 16a-c, with the temperature increasing from 80 to 180 °C, all membranes show higher performance. This can be attributed to the better mass transport as well as enhanced proton conductivity and reaction kinetic with higher working temperature [70]. Compared to the maximum power density

value of 0.07, 0.13, and 0.18 W/cm^2 of pure ABPBI membrane at 80, 120, and 180 °C, respectively, the expected improved performance has been shown with ABPBI/2S-Sep composite membrane with peak power density of 0.13, 0.18, and 0.23 W/cm^2. The peak power density of ABPBI/2S-Sep composite membrane based MEA at high temperature is higher than that of PBI/SiO_2 and PBI/clay membranes reported by Devrim et al. and Li et al., respectively [32, 79]; Moreover, the single cell performance at 80 °C with 0% RH can be comparable with the Nafion-based MEAs at 100 °C with 25% RH, 70 °C with 30% RH, 85 °C with 50% RH reported in literatures, respectively [34, 80, 81]. The remarkable power output ability of ABPBI/2S-Sep membrane based MEA is mainly due to the superior proton conductivity as well as excellent water absorption and PA retention properties of the composite membrane. Comparison of the PEMFC performances of MEAs prepared by net-ABPBI and ABPBI/2S-Sep membranes with near-identical thickness and PA DL shows that the single fuel cell with ABPBI/2S-Sep composite membrane has a prospect of PEMFCs application in a wide temperature range.

The short-term stability at constant voltage (0.6 V) of the ABPBI/2S-Sep composite membrane based HT-PEMFC at 180 °C under anhydrous condition is shown in Fig. 16d. Before the stability test, the MEA was subjected to an anhydrous state in order to remove the remaining water from the catalyst layers and membrane. During the test, the cell current was recorded every half minute. After the short-term performance for 10 h at 180 °C, the ABPBI/2S-Sep composite membrane based MEA follows a trend with a slightly decreasing cell current towards steady state, and the observed performance loss of the HT-PEMFC was obtained as 2.21%, which can be related to the formation of pyrophosphoric acid and further leads to the mass transfer

limitations [79, 82]. The MEA shows comparable performance with no signs of degradation within this preliminary test period indicating that the ABPBI/2S-Sep composite membrane has excellent durability and is quite suitable for HT-PEMFCs application.

4. Conclusions

ABPBI-based composite PEMs with the incorporation of sulfonated Sep were successfully prepared via *in-situ* synthesis followed by a solution casting technique. Through the treatment of acid activation, the Sep fibrous particles achieved a greatly increased specific surface area, pore volume of the micro-pores, amount of exposed Si–OH groups. Subsequent surface modification promoted the compatibility and provided a proton conducting pathway between Sep and ABPBI components, thus resulting in increased WU, PA DL, storage modulus, and proton conductivities. The best performances, especially with regard to proton conductivities in various temperatures and RH, were obtained for 2 wt.% of S-Sep incorporated ABPBI composite membranes. Benefitting from the fibrous shape and hygroscopic nature of Sep, these composite membranes showed additional and shortened proton paths as well as decreased E_a of proton transfer, thus showing excellent proton conductivities at low temperatures from 40-90 °C and RH from 0-98% RH. In addition, proton conductivities above 20% RH from the ABPBI/2S-Sep sample exceed 0.01 S/cm, and peak power density measured at 80 and 180 °C with anhydrous condition achieves 0.13 and 0.23 W/cm^2, respectively, indicating its potential as a promising candidate material for PEMFCs applied at a wide temperature range and without required humidity control.

Acknowledgments

This work was financially supported by the Hubei Provincial Natural Science Foundation Project (Grant No. 2017CFB575) and the Hubei Provincial Key Technology R&D Program (Grant Nos. 201710A01 and 201710A14). Dr. Chenxi Xu of Hefei University of Technology is thanked for his great help with the fuel cell tests.

References

[1] S. Srinivasan, Fuel cell from fundamentals to applications, Springer Science & Business media, (2006).

[2] K.D. Kreuer, Fuel cells: selected entries from the encyclopedia of sustainability science and technology, Springer New York, 2013.

[3] M. Rikukawa, K. Sanui, Proton-conducting polymer electrolyte membranes based on hydrocarbon polymers, Prog. Polym. Sci., 25 (2000) 1465-1502.

[4] D.W. Shin, M.D. Guiver, Y.M. Lee, Hydrocarbon-based polymer electrolyte membranes: importance of morphology on ion transport and membrane stability, Chem. Rev., 117 (2017) 4759-4805.

[5] M. Molleo, T.J. Schmidt, B.C. Benicewicz, Polybenzimidazole fuel cell technology, Springer New York, 2012.

[6] Q. Li, J.O. Jensen, R.F. Savinell, N.J. Bjerrum, High temperature proton exchange membranes based on polybenzimidazoles for fuel cells, Prog. Polym. Sci., 34 (2009) 449-477.

[7] P. Sun, Z. Li, L. Jin, Y. Yang, S. Wang, X. Yin, Y. Wang, Pre‐Oxidized Acrylic Fiber Reinforced Ferric Sulfophenyl Phosphate‐Doped Polybenzimidazole‐

Based High‐Temperature Proton Exchange Membrane, Macromol. Mater. Eng., 302 (2017) 1600468.

[8] P. Sun, Z. Li, F. Dong, S. Wang, X. Yin, Y. Wang, High temperature proton exchange membranes based on cerium sulfophenyl phosphate doped polybenzimidazole by end-group protection and hot-pressing method, Int J Hydrogen Energ, 42 (2017) 486-495.

[9] G.A. Giffin, S. Galbiati, M. Walter, K. Aniol, C. Ellwein, J. Kerres, R. Zeis, Interplay between structure and properties in acid-base blend PBI-based membranes for HT-PEM fuel cells, Journal of Membrane Science, 535 (2017) 122-131.

[10] K. Suzuki, Y. Iizuka, M. Tanaka, H. Kawakami, Phosphoric acid-doped sulfonated polyimide and polybenzimidazole blend membranes: high proton transport at wide temperatures under low humidity conditions due to new proton transport pathways, J. Mater. Chem., 22 (2012) 23767-23772.

[11] M. Schuster, C.C.D. Araujo, V. Atanasov, H.T. Andersen, K.D. Kreuer, J. Maier, Highly sulfonated poly(phenylene sulfone): preparation and stability issues, Macromolecules, 42 (2009) 3129-3137.

[12] K.S. Lee, J.S. Spendelow, Y.K. Choe, C. Fujimoto, Y.S. Kim, An operationally flexible fuel cell based on quaternary ammonium-biphosphate ion pairs, Nat. Energy, 1 (2016) 1-7.

[13] M.A. Hickner, H. Ghassemi, Y.S. Kim, B.R. Einsla, J.E. McGrath, Alternative polymer systems for proton exchange membranes (PEMs), Chem. Rev., 104

(2004) 4587-4611.

[14] Z.Y. Yue, Y.B. Cai, S.A. Xu, Phosphoric acid-doped organic-inorganic cross-linked sulfonated poly(imide-benzimidazole) for high temperature proton exchange membrane fuel cells, Int. J. Hydrog. Energy, 41 (2016) 10421-10429.

[15] K.D. Kreuer, On the complexity of proton conduction phenomena, Solid State Ionics, 136 (2000) 149-160.

[16] J.S. Wainright, J-T. Wang, D. Weng, R.F. Savinell, M. Litt, Acid-doped polybenzimidazoles a new polymer electrolyte, J. Electrochem. Soc., 142 (1995) 121-123.

[17] H.J. Kim, S.J. An, J.Y. Kim, K.M. Jin, S.Y. Cho, Y.C. Eun, H.K. Yoon, Y. Park, H.J. Kweon, E.M. Shin, Polybenzimidazoles for high temperature fuel cell applications, Macromol. Rapid Commun., 25 (2010) 1410-1413.

[18] Y.H. Jeong, K. Oh, S. Ahn, N.Y. Kim, A. Byeon, H.Y. Park, S.Y. Lee, H.S. Park, S.J. Yoo, J.H. Jang, H.J. Kim, H. Ju, J.Y. Kim, Investigation of electrolyte leaching in the performance degradation of phosphoric acid-doped polybenzimidazole membrane-based high temperature fuel cells, J. Power Sources, 363 (2017) 365-374.

[19] R.E. Rosli, A.B. Sulong, W.R.W. Daud, M.A. Zullzifley, T. Husaini, M.I. Rosli, E.H. Majlan, M.A. Haque, A review of high-temperature proton exchange membrane fuel cell (HT-PEMFC) system, Int. J. Hydrog. Energy, 42 (2017) 9293-9314.

[20] P. Sun, Z. Li, S. Wang, X. Yin, Performance enhancement of polybenzimidazole

based high temperature proton exchange membranes with multifunctional crosslinker and highly sulfonated polyaniline, Journal of Membrane Science, 549 (2018) 660-669.

[21] H. Zhang, P.K. Shen, Recent development of polymer electrolyte membranes for fuel cells, Chem. Rev., 112 (2012) 2780-2832.

[22] D.J. Kim, M.J. Jo, S.Y. Nam, A review of polymer-nanocomposite electrolyte membranes for fuel cell application, J. Ind. Eng. Chem., 21 (2015) 36-52.

[23] A. Kraytsberg, Y. Ein-Eli, Review of advanced materials for proton exchange membrane fuel cells, Energy & Fuels, 28 (2014) 7303-7330.

[24] P. Sun, Z. Li, L. Jin, S. Wang, X. Yin, Construction of proton channels and reinforcement of physicochemical properties of oPBI/FeSPP/GF high temperature PEM via building hydrogen bonding network, Int. J. Hydrog. Energy, (2017).

[25] P. Sun, Z. Li, M. Song, S. Wang, X. Yin, Y. Wang, Preparation and characterization of zirconium phytate as a novel solid intermediate temperature proton conductor, Mater. Lett., 191 (2017) 161-164.

[26] S.W. Wang, P. Sun, Z.F. Li, G.H. Liu, X.Y. Yin, Comprehensive performance enhancement of polybenzimidazole based high temperature proton exchange membranes by doping with a novel intercalated proton conductor, Int. J. Hydrog. Energy, 43 (2018) 9994-10003.

[27] J. Zhang, D. Aili, J. Bradley, H. Kuang, C. Pan, R. De Marco, Q. Li, S.P. Jiang, In situ formed phosphoric acid/phosphosilicate nanoclusters in the exceptional

enhancement of durability of polybenzimidazole membrane fuel cells at elevated high temperatures, J. Electrochem. Soc., 164 (2017) F1615-F1625.

[28] T.J. Schmidt, Durability and degradation in high-temperature polymer electrolyte fuel cells, ECS transactions, 1 (2006) 19-31.

[29] T.J. Schmidt, High-temperature polymer electrolyte fuel cells: durability insights, Springer New York, 2009.

[30] Q. Li, D. Aili, H.A. Hjuler, J.O. Jensen, High temperature polymer electrolyte membrane fuel cells, chapter 13: PBI-based composite membranes, Springer International Publishing, 2016.

[31] A.K. Mishra, S. Bose, T. Kuila, N.H. Kim, J.H. Lee, Silicate-based polymer-nanocomposite membranes for polymer electrolyte membrane fuel cells, Prog. Polym. Sci., 37 (2012) 842-869.

[32] D. Plackett, A. Siu, Q. Li, C. Pan, J.O. Jensen, S.F. Nielsen, A.A. Permyakova, N.J. Bjerrum, High-temperature proton exchange membranes based on polybenzimidazole and clay composites for fuel cells, Journal of Membrane Science, 383 (2011) 78-87.

[33] C. Beauger, G. Laine, A. Burr, A. Taguet, B. Otazaghine, Improvement of Nafion®-sepiolite composite membranes for PEMFC with sulfo-fluorinated sepiolite, Journal of Membrane Science, 495 (2015) 392-403.

[34] C. Beauger, G. Lainé, A. Burr, A. Taguet, B. Otazaghine, A. Rigacci, Nafion®-sepiolite composite membranes for improved proton exchange membrane fuel cell performance, Journal of Membrane Science, 430 (2013)

167-179.

[35] F.J. Fernandez-Carretero, K. Suarez, O. Solorza, E. Riande, V. Compan, PEMFC Performance of MEAS Based on Nafion (R) AND sPSEBS Hybrid Membranes, J. New Mat. Electr. Sys., 13 (2010) 191-199.

[36] F.J. Fernandez-Carretero, E. Riande, C. del Rio, F. Sanchez, J.L. Acosta, V. Compan, Preparation and Characterization of Hybrid Membranes based on Nafion (R) using Partially Sulfonated Inorganic Fillers, J. New Mat. Electr. Sys., 13 (2010) 83-93.

[37] M. Oroujzadeh, S. Mehdipour-Ataei, M. Esfandeh, Microphase separated sepiolite-based nanocomposite blends of fully sulfonated poly(ether ketone)/non-sulfonated poly(ether sulfone) as proton exchange membranes from dual electrospun mats, RSC. Adv., 5 (2015) 72075-72083.

[38] S. Sasikala, S. Meenakshi, S.D. Bhat, A.K. Sahu, Functionalized bentonite clay-sPEEK based composite membranes for direct methanol fuel cells, Electrochim. Acta, 135 (2014) 232-241.

[39] D.J. Kim, H.Y. Hwang, S.B. Jung, S.Y. Nam, Sulfonated poly(arylene ether sulfone)/laponite-SO3H composite membrane for direct methanol fuel cell, J. Ind. Eng. Chem., 18 (2012) 556-562.

[40] X. Bao, F. Zhang, Q. Liu, Sulfonated poly(2,5-benzimidazole) (ABPBI)/MMT/ionic liquids composite membranes for high temperature PEM applications, Int. J. Hydrog. Energy, 40 (2015) 16767-16774.

[41] J.J.R. Arias, J.C. Dutra, A.D. Gomes, Hybrid membranes of sulfonated poly ether

ether ketone, ionic liquid and organically modified montmorillonite for proton exchange membranes with enhanced ionic conductivity and ionic liquid lixiviation protection, Journal of Membrane Science, 537 (2017) 353-361.

[42] F. Xu, S. Mu, M. Pan, Mineral nanofibre reinforced composite polymer electrolyte membranes with enhanced water retention capability in PEM fuel cells, Journal of Membrane Science, 377 (2011) 134-140.

[43] G. Tartaglione, D. Tabuani, G. Camino, Thermal and morphological characterisation of organically modified sepiolite, Micropor. Mesopor. Mat., 107 (2008) 161-168.

[44] C.H. Zhou, G.L. Li, X.Y. Zhuang, P.P. Wang, D.S. Tong, H.M. Yang, C.X. Lin, L. Li, H. Zhang, S.F. Ji, W.H. Yu, Roles of texture and acidity of acid-activated sepiolite catalysts in gas-phase catalytic dehydration of glycerol to acrolein, Mol. Catal., 434 (2017) 219-231.

[45] F. Zhou, C.J. Yan, Y. Zhang, J.J. Tan, H.Q. Wang, S. Zhou, S. Pu, Purification and defibering of a Chinese sepiolite, Appl Clay Sci, 124 (2016) 119-126.

[46] J. Ouyang, W. Gu, C. Zheng, H. Yang, X. Zhang, Y. Jin, J. Chen, J. Jiang, Polyethyleneimine (PEI) loaded MgO-SiO2 nanofibers from sepiolite minerals for reusable CO2 capture/release applications, Appl Clay Sci, 152 (2018) 267-275.

[47] F. Liu, S. Wang, J. Li, X. Tian, X. Wang, H. Chen, Z. Wang, Polybenzimidazole/ionic-liquid-functional silica composite membranes with improved proton conductivity for high temperature proton exchange membrane

fuel cells, Journal of Membrane Science, 541 (2017) 492-499.

[48] Q. Liu, Q. Sun, N. Ni, F. Luo, R. Zhang, S. Hu, X. Bao, F. Zhang, F. Zhao, X. Li, Novel octopus shaped organic–inorganic composite membranes for PEMFCs, Int. J. Hydrog. Energy, 41 (2016) 16160-16166.

[49] S. Singha, T. Jana, Influence of interfacial interactions on the properties of polybenzimidazole/clay nanocomposite electrolyte membrane, Polymer, 98 (2016) 20-31.

[50] X. Tian, S. Wang, J.S. Li, F.X. Liu, X. Wang, H. Chen, H.Z. Ni, Z. Wang, Composite membranes based on polybenzimidazole and ionic liquid functional Si-O-Si network for HT-PEMFC applications, Int. J. Hydrog. Energy, 42 (2017) 21913-21921.

[51] Q. Shen, J. Ouyang, Y. Zhang, Lauric acid/modified sepiolite composite as a form-stable phase change material for thermal energy storage, Appl Clay Sci, 146 (2017) 14-22.

[52] F. Franco, M. Pozo, J.A. Cecilia, M. Benitez-Guerrero, E. Pozo, J.A.M. Rubi, Microwave assisted acid treatment of sepiolite: The role of composition and "crystallinity", Appl Clay Sci, 102 (2014) 15-27.

[53] B.E. Alver, Hydrogen adsorption on natural and sulphuric acid treated sepiolite and bentonite, Int. J. Hydrog. Energy, 43 (2018) 831-838.

[54] S.Q. Zheng, Y. Han, X.H. Huang, Y.L. Dai, D. Qian, J.C. Zhang, S. Ren, Acid and aluminium modification of sepiolite and its application in FCC catalysis, Clay Miner., 45 (2010) 15-22.

[55] N. Alan, S. İşçi, Surface modification of sepiolite particles with polyurethane and polyvinyl alcohol, Prog. Org. Coat., 77 (2014) 444-448.

[56] M. Alkan, G. Tekin, H. Namli, FTIR and zeta potential measurements of sepiolite treated with some organosilanes, Micropor. Mesopor. Mat., 84 (2005) 75-83.

[57] M. Suarez, J. Garcia-Rivas, E. Garcia-Romero, N. Jara, Mineralogical characterisation and surface properties of sepiolite from Polatli (Turkey), Appl Clay Sci, 131 (2016) 124-130.

[58] K. Seo, J. Seo, K.H. Nam, H. Han, Polybenzimidazole/inorganic composite membrane with advanced performance for high temperature polymer electrolyte membrane fuel cells, Polym. Compos., 38 (2017) 87-95.

[59] L.L. Mao, A.K. Mishra, N.H. Kim, J.H. Lee, Poly(2,5-benzimidazole)-silica nanocomposite membranes for high temperature proton exchange membrane fuel cell, Journal of Membrane Science, 411 (2012) 91-98.

[60] N.N. Krishnan, S. Lee, R.V. Ghorpade, A. Konovalova, J.H. Jang, H.J. Kim, J. Han, D. Henkensmeier, H. Han, Polybenzimidazole (PBI-OO) based composite membranes using sulfophenylated TiO2 as both filler and crosslinker, and their use in the HT-PEM fuel cell, Journal of Membrane Science, 560 (2018) 11-20.

[61] X. Liang, Y. Xu, G. Sun, L. Wang, Y. Sun, S. Yang, Q. Xu, Preparation and characterization of mercapto functionalized sepiolite and their application for sorption of lead and cadmium, Chem. Eng. J., 174 (2011) 436-444.

[62] M. Kulkarni, R. Potrekar, R.A. Kulkarni, S.P. Vernekar, Synthesis and characterization of novel polybenzimidazoles bearing pendant phenoxyamine

groups, J. Polym. Sci., Part A: Ploym. Chem., 46 (2008) 5776-5793.

[63] S. Singha, T. Jana, Structure and properties of polybenzimidazole/silica nanocomposite electrolyte membrane: influence of organic/inorganic interface, ACS Appl. Mater. Inter., 6 (2014) 21286-21296.

[64] Y. Özdemir, N. Üregen, Y. Devrim, Polybenzimidazole based nanocomposite membranes with enhanced proton conductivity for high temperature PEM fuel cells, Int. J. Hydrog. Energy, 42 (2016) 2648-2657.

[65] A.K. Mishra, N.H. Kim, J.H. Lee, Effects of ionic liquid-functionalized mesoporous silica on the proton conductivity of acid-doped poly(2,5-benzimidazole) composite membranes for high-temperature fuel cells, Journal of Membrane Science, 449 (2014) 136-145.

[66] J. Lobato, P. Cañizares, M.A. Rodrigo, D. Ubeda, F.J. Pinar, Promising TiOSO4 composite polybenzimidazole-based membranes for high temperature PEMFCs, Chemsuschem, 4 (2011) 1489-1497.

[67] Y.D. Zhang, L.J. Wang, F. Wang, J.S. Liang, S.S. Ran, J.F. Sun, Phase transformation and morphology evolution of sepiolite fibers during thermal treatment, Appl Clay Sci, 143 (2017) 205-211.

[68] J. Cho, J. Blackwell, S.N. Chvalun, M. Litt, Y. Wang, Structure of a poly(2,5 - benzimidazole)/phosphoric acid complex, J. Polym. Sci., Part B: Ploym. Phys., 42 (2004) 2576-2585.

[69] S. Maity, S. Singha, T. Jana, Low acid leaching PEM for fuel cell based on polybenzimidazole nanocomposites with protic ionic liquid modified silica,

Polymer, 66 (2015) 76-85.

[70] J. Dang, L. Zhao, J. Zhang, J. Liu, J. Wang, Imidazole microcapsules toward enhanced phosphoric acid loading of polymer electrolyte membrane for anhydrous proton conduction, Journal of Membrane Science, 545 (2018) 88-98.

[71] J. Hao, Y. Jiang, X. Gao, W. Lu, Y. Xiao, Z. Shao, B. Yi, Functionalization of polybenzimidazole-crosslinked poly(vinylbenzyl chloride) with two cyclic quaternary ammonium cations for anion exchange membranes, Journal of Membrane Science, 548 (2018) 1-10.

[72] Suryani, Y.L. Liu, Preparation and properties of nanocomposite membranes of polybenzimidazole/sulfonated silica nanoparticles for proton exchange membranes, Journal of Membrane Science, 332 (2009) 121-128.

[73] C.H. Shen, S.L.C. Hsu, E. Bulycheva, N. Belomoina, Polybenzimidazole/1H-imidazole-4-sulfonic acid hybrid membranes for high-temperature proton exchange membranes fuel cells, Journal of Membrane Science, 399 (2012) 11-15.

[74] L.C. Jheng, C.Y. Huang, S.L.C. Hsu, Sulfonated MWNT and imidazole functionalized MWNT/polybenzimidazole composite membranes for high-temperature proton exchange membrane fuel cells, Int. J. Hydrog. Energy, 38 (2013) 1524-1534.

[75] A. Eguizabal, J. Lemus, M.P. Pina, On the incorporation of protic ionic liquids imbibed in large pore zeolites to polybenzimidazole membranes for high temperature proton exchange membrane fuel cells, J. Power Sources, 222 (2013)

483-492.

[76] Q.T. Che, R.H. He, J.S. Yang, L. Feng, R.F. Savinell, Phosphoric acid doped high temperature proton exchange membranes based on sulfonated polyetheretherketone incorporated with ionic liquids, Electrochem. Commun., 12 (2010) 647-649.

[77] R. Bouchet, E. Siebert, Proton conduction in acid doped polybenzimidazole, Solid State Ionics, 118 (1999) 287-299.

[78] C. Xu, X. Liu, J. Cheng, K. Scott, A polybenzimidazole/ionic-liquid-graphite-oxide composite membrane for high temperature polymer electrolyte membrane fuel cells, J. Power Sources, 274 (2015) 922-927.

[79] Y. Devrim, H. Devrim, I. Eroglu, Polybenzimidazole/SiO2 hybrid membranes for high temperature proton exchange membrane fuel cells, Int. J. Hydrog. Energy, 41 (2016) 10044-10052.

[80] A. D'Epifanio, M.A. Navarra, F.C. Weise, B. Mecheri, J. Farrington, S. Licoccia, S. Greenbaum, Composite nafion/sulfated zirconia membranes: effect of the filler surface properties on proton transport characteristics, Chem. Mater., 22 (2009) 813-821.

[81] Y. Devrim, A. Albostan, Enhancement of PEM fuel cell performance at higher temperatures and lower humidities by high performance membrane electrode assembly based on Nafion/zeolite membrane, Int. J. Hydrog. Energy, 40 (2015) 15328-15335.

[82] Y. Devrim, A. Albostan, H. Devrim, Experimental investigation of CO tolerance in high temperature PEM fuel cells, Int. J. Hydrog. Energy, 43 (2018) 18672-18681.

Highlights:

- Sepiolite nanoparticles with high specific surface area and porosity are synthesized.
- Proton conductivity of ABPBI/2S-Sep is above 0.01 S/cm at 40-180 °C with RH ≥ 20%.
- High proton conductivity is due to the multi-conduction paths of composites.